Global Change Biology

WILEY

Global Change Biology

RESEARCH ARTICLE OPEN ACCESS

Global Flux-Based Assessment Reveals Declining Ozone Risk for Wheat in Future Climate Change Scenarios

Pierluigi R. Guaita[1,2] | Riccardo Marzuoli[1] | Leiming Zhang[3] | Steven Turnock[4,5] | Gerbrand Koren[6] | Oliver Wild[7] | Paola Crippa[8] | Giacomo Gerosa[1]

[1]Department of Mathematics and Physics, Catholic University of the Sacred Heart, Brescia, Italy | [2]Department of Applied Computational Mathematics and Statistics, University of Notre Dame, Notre Dame, Indiana, USA | [3]Air Quality Research Division, Science and Technology Branch, Environment and Climate Change Canada, Toronto, Canada | [4]Met Office Hadley Centre, Exeter, UK | [5]University of Leeds Met Office Strategic (LUMOS) Research Group, University of Leeds, UK | [6]Copernicus Institute of Sustainable Development, Utrecht University, Utrecht, the Netherlands | [7]Lancaster Environment Centre, Lancaster University, Lancaster, UK | [8]Department of Civil and Environmental Engineering and Earth Sciences, University of Notre Dame, Notre Dame, Indiana, USA

Correspondence: Pierluigi R. Guaita (pierluigirenan.guaita@unicatt.it) | Giacomo Gerosa (giacomo.gerosa@unicatt.it)

Received: 15 May 2025 | **Revised:** 1 November 2025 | **Accepted:** 15 November 2025

Keywords: CMIP6 | CO_2 | dry deposition | ESM | food security | POD_6 | SSP | stomatal conductance | yield loss

ABSTRACT

Tropospheric ozone (O_3) is a widespread air pollutant that impairs crop physiology and threatens global food security. Most global-scale assessments have relied on exposure-based metrics, which overlook plant–environment interactions that control O_3 uptake. This study presents a global flux-based assessment of future O_3 risk for wheat (*Triticum aestivum*) using a dual-sink dry deposition model driven by Earth System Models from the Coupled Model Intercomparison Project 6 (CMIP6) under three Shared Socioeconomic Pathways (SSP1-2.6, SSP3-7.0, and SSP5-8.5). We quantify phytotoxic O_3 dose (POD_6) and production losses from 2000 to 2100, analyze regional trends, and perform multiple simulations to assess the influence of soil water availability and atmospheric CO_2 on O_3 risk. Finally, we explore the roles of radiative forcing (RF), emission policies on O_3 precursors (EP), and their interaction, in determining O_3 risk changes. We find a general decline in O_3 risk, although regional disparities remain. Under SSP1-2.6 (strong EP, low RF) POD_6 declines throughout the century, leading global mean production losses to decrease from 3.3% to 5.0% at the beginning of the century to less than 1.4% at its end. In contrast, SSP3-7.0 (weak EP, high RF) shows end-century losses between 1.3% and 4.9% and may exacerbate risks in several regions (South and East Asia, South America, Sub-Saharan Africa). SSP5-8.5 displays intermediate outcomes: O_3 risk increases until mid-century in many regions, and then declines by 2100 (0.5%–2.6%), due to delayed EP adoption. Increasing atmospheric CO_2 concentrations will likely hinder future O_3 risk due to reduced stomatal conductance, but some hotspots will persist near the Southern and Eastern edges of the Tibetan Plateau. These findings provide a basis for prioritizing region-specific mitigation strategies to reduce O_3 damage to wheat under future climate conditions.

1 | Introduction

Tropospheric ozone (O_3) poses a significant threat to global crop production in a changing climate, with potentially serious implications for worldwide food security. With rising greenhouse gas concentrations and shifting emission patterns projected throughout the 21st century, understanding how these environmental changes will affect vital food crops and their response to O_3 becomes increasingly important for agricultural planning and policy decisions.

O_3 damages vegetation by entering the leaf through stomata and altering key biogeochemical and physiological processes, resulting in reduced photosynthesis, accelerated leaf senescence, and causing the expression of detoxification systems. This in turn reduces canopy carbon gain and biodiversity, among other negative effects (Fuhrer et al. 2016; Grulke and Heath 2020; Ramya et al. 2023; Wright et al. 2018), and has important consequences for food security (Emberson 2020).

The quantification of O_3 impacts on vegetation can be achieved through two distinct methodologies: an exposure (concentration)-based approach and a dose (flux)-based approach. Several studies have compared the two approaches across a wide range of vegetation types (Anav et al. 2016; Hoshika et al. 2020; Karlsson et al. 2007; Mao et al. 2024; Mills et al. 2018; Paoletti et al. 2019; Pleijel et al. 2022; Simpson et al. 2007; Tai et al. 2021; Tang et al. 2014). These comparisons consistently highlight that the flux-based approach, which estimates the phytotoxic ozone dose (POD), better represents the biological processes leading to O_3 damage to vegetation, as it accounts for the amount of O_3 entering the plants through the stomata (Paoletti and Manning 2007). Existing schemes for estimating O_3 stomatal flux to vegetation vary in complexity, ranging from a simple function of temperature and solar radiation (Wesely 1989), to a single leaf Jarvis model (Baldocchi et al. 1987; Jarvis 1976), a sunlit/shade (two-big-leaf) scheme (Emberson, Ashmore, et al. 2000; Zhang et al. 2003), and a photosynthesis approach (Ball et al. 1987; Charusombat et al. 2010). Combined models that integrate elements from the above-mentioned schemes have also been developed (Clifton et al. 2023; and references therein).

Regional- to global-scale O_3 risk assessments for various vegetation types have been extensively conducted over the past two decades, using both exposure-based and flux-based approaches to estimate past and present O_3 damage (Anav et al. 2011; Cheesman et al. 2023; Guaita et al. 2023; Mills et al. 2011, 2018; Savi et al. 2020; Sharps, Hayes, et al. 2021; Van Dingenen et al. 2009). Many of these studies concluded that high O_3 concentrations can cause significant crop yield losses and economic damages worldwide (Pleijel et al. 2018; Tai et al. 2021).

However, studies of future O_3 impacts on vegetation have mostly applied exposure-based methods (e.g., Chuwah et al. 2015; Sicard et al. 2017). The few studies that have explicitly adopted flux-based approaches to estimate future O_3 impacts, have typically simplified assumptions, such as applying present-day meteorology with projected emissions, or present-day emissions with future climate (Klingberg et al. 2014; Simpson et al. 2007; Tang et al. 2014). To our knowledge, a comprehensive, global flux-based analysis of O_3 impacts across the 21st century, considering both future climate and emission scenarios, is still lacking. A key aspect in O_3 risk assessment over future times is the accurate consideration of the effect of rising atmospheric CO_2 concentrations on plant physiology and O_3 uptake. Elevated CO_2 levels typically induce partial stomatal closure in C3 crops like wheat, potentially reducing O_3 uptake and subsequent damage. This CO_2-induced effect reflects a complex physiological interaction of plant responses: while increased CO_2 may enhance photosynthesis and water use efficiency, it simultaneously provides a protective effect against O_3 damage by limiting stomatal conductance (Ainsworth et al. 2012; Fiscus et al. 2005). However, this protective effect is complicated by other climate factors, as changes in temperature, vapor pressure deficit and water stress may counteract stomatal closure. The net effect of these interacting variables will likely differ across geographic regions depending on their specific climatic conditions.

This study addresses these research gaps through a global-scale, flux-based assessment of future O_3 risks for bread wheat (*Triticum aestivum*), which is one of the world's most important staple food crops and a reference for agricultural species with high O_3-sensitivity (Mills et al. 2011; Sitch et al. 2007). More specifically, the objectives of this research are to: (1) estimate future trends of POD for wheat to the end of the 21st century under different climate change scenarios; (2) identify the regions that are most vulnerable to future food security threats due to the negative O_3 effects on wheat; (3) evaluate the impact of different adaptation and mitigation strategies in reducing future O_3 risk.

To address these objectives, we employ a dual-sink big-leaf dry deposition model (Guaita et al. 2023), driven by meteorology and O_3 concentration outputs from Earth System Models (ESMs) participating in the Coupled Model Intercomparison Project 6 (CMIP6; Eyring et al. 2016). To generate a set of future climate simulations, these ESMs use the forcing datasets associated with the "shared socioeconomic pathways" (SSP; Riahi et al. 2017), which are future pathways combining different trends in social, economic and environmental developments with different assumptions about anthropogenic emission mitigation applied on top of these to meet pre-defined climate targets (radiative forcing; RF).

2 | Methodology

2.1 | Selection of CMIP6 Models and SSPs

A subset of models from the CMIP6 experiment is selected as input for this work. Specifically, we apply the following criteria to identify the model runs suitable for our study: (i) an online/coupled-chemistry framework (AerChemMIP; Collins et al. 2017) to include the feedback of O_3 on climate and (ii) sub-daily temporal resolution of meteorological variables to enable O_3 flux calculations. According to these criteria, we identify GFDL-ESM4 (Dunne et al. 2020; Horowitz et al. 2018; Krasting et al. 2018) and UKESM1-0-LL (O'Connor 2020; Sellar et al. 2019; Tang et al. 2019) for this study. UKESM1-0-LL and GFDL-ESM4 are both fully coupled global ESMs, which include a physical atmosphere–ocean model coupled with additional interactive earth system components including ocean biogeochemistry, stratosphere-troposphere chemistry and aerosol scheme and terrestrial carbon cycles coupled to interactive vegetation (Table S1). They both have a horizontal grid resolution of between 100 and 140 km in the mid-latitudes, with vertical levels extending to the upper stratosphere. Comprehensive chemistry schemes are included within both ESMs simulating the reactions and transport of major chemical species involved in O_3 formation. As a result, these ESMs can simulate the interactions between climate and chemistry changes across both historical and future periods. The model variables required for this study are listed in Table S1. POD calculations require O_3 concentrations

to be scaled from the model level geometric height to the canopy height, which is achieved using the dry deposition model used in this study (Guaita et al. 2023). See Appendix SA.1 for details.

Annual O_3 risk for wheat from 2015 to 2100 is quantified relative to a POD baseline value, calculated as the average over the 2000–2014 period. The POD for the baseline years is derived from the "historical" experiment of CMIP6 (Eyring et al. 2016). Future O_3 risk is estimated based on climate and emission scenarios described by the SSPs (Riahi et al. 2017). Specifically, we focus on the scenarios SSP1-2.6 (Van Vuuren et al. 2017), SSP3-7.0 (Fujimori et al. 2017), and SSP5-8.5 (Kriegler et al. 2017), as they represent contrasting characteristics in terms of future RF and emission policies (EP) for air quality that impact O_3 concentrations from 2015 to 2100. Herein we classify SSP1-2.6 as a low-emissions and low-RF scenario, SSP3-7.0 as a high-emissions and high-RF scenario, while SSP5-8.5 as a high-RF and partial emission control scenario, with controls beginning in the second half of the 21st Century. Thus, from an O_3 concentration perspective, SSP5-8.5 can be broadly considered as an intermediate scenario, with end-of-century pronounced climate change and O_3 concentrations akin to those observed in the historical baseline (Turnock et al. 2020). Further, the SSP3-7.0pdSST experiment (present-day Sea Surface Temperature; Zanis et al. 2022) is available from UKESM1-0-LL and is included in this study to assess the effect of changing O_3 concentrations only in a high-emission/present-day climate scenario. ESM outputs show biases in both meteorological variables and O_3 concentrations. An evaluation of the O_3 bias against the surface O_3 observations from the Tropospheric Ozone Assessment Report (TOAR) dataset (Schröder et al. 2021) for the baseline years (2000–2014) is presented in the Appendix (SA.2), alongside the effect of meteorological and O_3 biases on the final POD estimate.

2.2 | Dry Deposition Model for Wheat

The POD calculations follow the approach described in the LRTAP Convention (2017). More specifically, we use a dual-sink big-leaf O_3 dry deposition model that calculates stomatal conductance (g_s) and O_3 uptake by plants, following the DO3SE paradigm originally developed by Emberson, Ashmore, et al. (2000). This model also simulates phenology, soil water available to the plant, and light penetration within the canopy, and accounts for atmospheric stability and instability with the Monin-Obukhov similarity theory along with a resistive scheme. The O_3 stomatal flux model receives as input meteorological and chemical data from the CMIP6 models under the different SSPs. The complete formulation of the O_3 dry deposition model is described in the Appendix SB of Guaita et al. (2023). Modifications applied in this study are detailed in Appendix (SA.3).

O_3 deposition from the lowest model level to the vegetated surface is calculated with a resistive network of three resistances (bulk resistances, uppercase R) in series: an atmospheric resistance R_a, a quasi-laminar sublayer resistance R_b, and a surface resistance R_c. The latter consists of three resistances in parallel: a cuticular resistance R_{cut}, a stomatal resistance R_{stom} and a ground resistance composed of an intra-canopy resistance R_{inc} and a soil resistance R_{soil}, in series. Following the DO3SE methodology (Emberson, Ashmore, et al. 2000; Emberson, Simpson, et al. 2000), the canopy-level resistance R_{stom} is obtained by upscaling the leaf-level resistances (lowercase r), while accounting for sunlit and shaded portion of the canopy. On the other hand, only the stomatal resistance for a sunlit upper canopy leaf is used to calculate the stomatal O_3 uptake. The leaf-level stomatal resistance is calculated as the inverse of the stomatal conductance g_s, obtained by applying the empirical Jarvis-Stewart approach (Jarvis 1976; Stewart 1988):

$$g_s = g_{max} \times \min\left\{f_{phen}, f_{O_3}\right\} \times f_{light} \times \max\left\{f_{min}, f_{temp} \times f_{VPD} \times f_{soil}\right\} \times f_{CO_2} \quad (1)$$

where the f functions (ranging between 0 and 1) are taken directly from the LRTAP Convention (2017), with the only exception of f_{CO_2} (see below). The f functions describe the limiting effect on g_{max} due to light (f_{light}), temperature (f_{temp}), air water Vapour Pressure Deficit (f_{VPD}) and soil water available to the plant (f_{soil}), and to phenological growth (f_{phen}) and O_3 dose received by the plants (f_{O3}). For this study an f_{clim} term is defined as the product $f_{temp} \times f_{VPD} \times f_{soil}$ to represent the combined effect of the main climatic factors on g_s. The f_{min} term represents a constant value of 0.01 indicating the minimum g_s expressed relative to g_{max} during daylight hours.

In addition to the LRTAP Convention (2017) methodology, the f_{CO_2} function was defined to describe how g_s is affected by CO_2 concentrations, which are projected to further increase in the next decades until the end of the century. In fact, increasing CO_2 concentrations are known to decrease g_s non-linearly (Franks et al. 2017; Haworth et al. 2016; Li et al. 2019). The relationship between rising CO_2 concentrations and the penalty on g_{max} can be represented with the equation:

$$f_{CO_2}\left([CO_2]\right) = f_{min,CO_2} + \left(1 - f_{min,CO_2}\right) \times \exp\left(- a_{CO_2} \times \frac{[CO_2] - CO_{2,ref}}{CO_{2,ref}} \right) \quad (2)$$

where a_{CO_2} is a shape parameter, $CO_{2,ref}$ ([ppm]) is the reference CO_2 concentration to which $f_{CO_2} = 1$, and f_{min,CO_2} is the minimum fractional value of g_{max} that can be reached by increasing CO_2 concentrations. The values for a_{CO_2}, f_{min,CO_2} and $CO_{2,ref}$ are inferred from the output of a FvCB model for photosynthesis (Farquhar-von Caemmerer-Berry; Farquhar et al. 1980) coupled with a Ball-Berry scheme for g_s (Ball et al. 1987) applied to winter wheat in non-limiting water conditions and optimal light, humidity and air temperature, accounting for diurnal g_s maxima at increasing ambient concentration of CO_2 from 380 to 1000 ppm. Inference on the simulation outputs led to $a_{CO_2} = 0.5480$ (95% CI: 0.4978, 0.5982), $f_{min,CO_2} = 0.2823$ (95% CI: 0.2449, 0.3196), and $CO_{2,ref} = 384.2$ ppm (95% CI: 380.0, 388.4). This relationship (Figure S1) was found to be consistent with several experimental studies and reviews (Agrawal and Deepak 2003; Ainsworth and Rogers 2007; Del Pozo et al. 2005; Kang et al. 2021; Tuba et al. 1994).

The O_3 dry deposition model varies leaf area index, surface area index, crop height, and root depth according to the growth stage and phenology of wheat. Soil water is simulated at each timestep with a vertical water budget model that, following the methodology of Mintz and Walker (1993), accounts for precipitation, canopy transpiration, evaporation from soil and wet surfaces,

and throughfall (Guaita et al. 2023). Sowing date maps and soil hydraulic properties (wilting point and field capacity soil maps) are required by the model. The sowing date maps are from Qiao et al. (2023), who produced a global dataset for *T. aestivum* for SSP1-2.6 and SSP3-7.0. The soil texture maps are used to simulate soil water available to the plant during the growing season and they are obtained from Zhang et al. (2018). An evaluation of the dry deposition model against FLUXNET data (Fischer et al. 2007; Lohila et al. 2004; Moureaux et al. 2006; Pastorello et al. 2020; Raz-Yaseef et al. 2015) and O_3 flux measurements over a wheat field (Gerosa et al. 2003) is shown in the Appendix (SA.4).

For the simulations in this work, different parameterizations of g_s for *T. aestivum* are adopted depending on the different biogeographical regions (Table S2). In the context of sowing dates, Qiao et al. (2023) categorized wheat-growing areas into four climatic zones (temperate, cold, warm, and monsoon) based on the seasonality of temperature and precipitation. According to this classification, we use the wheat parameterizations of the Mapping Manual (MM; LRTAP Convention 2017) for the g_s model. Depending on the climatic zone, we select the following parameterizations: spring wheat (Grünhage et al. 2012) in the cold region, winter wheat (Grünhage et al. 2012) in the temperate region, and mediterranean wheat (González-Fernández et al. 2013) in the warm and monsoon regions.

Once g_s is obtained, the seasonal O_3 stomatal dose received by wheat plants can be calculated as the phytotoxic O_3 dose above the Y threshold accounting for plants detoxification capacity (POD_Y; mmol O_3 m^{-2} of PLA, projected leaf area) by integrating the hourly O_3 stomatal flux ($F_{sO_3,i}$; nmol O_3 $m^{-2}s^{-1}$) over the flux accumulation period ($i = 0, \ldots t$, i-th hour of the accumulation period):

$$POD_Y = \sum_{i=0}^{t} \max\left\{F_{sO_3,i} - Y, 0\right\} \times 3600 \times 10^{-6} \quad (3)$$

$F_{sO_3,i}$ is obtained from the O_3 concentration at top canopy height $O_3(h_c)$:

$$F_{sO_3,i} = O_3(h_c) \times \frac{1}{r_s} \times \left(1 - \frac{r_b}{r_b + r_c}\right) \quad (4)$$

where r_s, r_b and r_c are the leaf-level stomata resistance, the quasi-laminar resistance and the leaf surface resistance (see Appendix in Guaita et al. 2023).

For *T. aestivum* a detoxifying threshold of 6 nmol O_3 $m^{-2}s^{-1}$ (POD_6) is recommended by the LRTAP Convention (2017), and the accumulation period for POD_6 is defined as the timespan between the unrolling of the flag leaf (shortly before anthesis) and crop maturity. The wheat parameterizations adopted in the MM use thermal time (growing degree days) to identify the accumulation period, with January 1st as the reference date for calculations in the Northern Hemisphere. However, to account for the different seasonality in the two hemispheres, we use the sowing date as the reference date instead. Thus, the phenological parameterizations as defined in the MM are adjusted by adding the thermal time that typically accumulates between the sowing date and the 1st of January. This value was estimated at 550°C days in Guaita et al. (2023), and is confirmed in the present work by comparing it with the thermal times calculated from the sowing dates provided by Qiao et al. (2023) up to the 1st of January. Following this adjustment, the thermal times for maturity are set to 1775°C, 2325°C and 2400°C days for spring wheat, winter wheat and Mediterranean wheat, respectively. The other parameters of the phenological function are shifted accordingly. An evaluation of the phenological stages based on thermal time and sowing date was carried out by comparison against two independent products (Global Gridded Model Intercomparison Project Crop Calendar, Jägermeyr et al. 2021; ChinaCropPhen1km, Luo et al. 2020) and is shown in the Appendix (SA.5).

A dose–response relationship for *T. aestivum* based on POD_6 and relative grain yield (Grünhage et al. 2012; LRTAP Convention 2017; Pleijel et al. 2007) can be used to calculate the relative yield loss (RYL; %):

$$RYL = 3.85 \times POD_6 \quad (5)$$

This relationship predicts a 5% decrease of grain yield for each increment of O_3 dose of 1.3 mmol m^{-2} PLA, and this is defined as the "Critical Level" (CL).

2.3 | Dry Deposition Model Runs, Assumptions, and Output Analysis

Four runs are presented in this study. The first run estimates POD_6 for the O_3 risk assessment, consistently with a common framework defined by the LRTAP Convention (2017), and is therefore labeled as "MM run" (Mapping Manual). Soil water available to the plant is assumed at field capacity at the sowing date every year and is dynamically simulated using an online water budget model. In this run, $f_{CO_2} = 1$ at every timestep. The second run (henceforth "MM + CO2 run") simulates soil water availability as the MM run but calculates f_{CO_2} according to Equation (2). This allows estimation of the changes in POD_6 due to the reductions of g_{max} at elevated CO_2 concentrations, while accounting for the feedback that the reduced g_s has on transpiration. The MM and the MM + CO_2 runs assume no irrigation, and therefore they are labeled also as "rainfed runs". The third and fourth run (henceforth "MM_FC run" and "MM + CO_2_FC run") aim to diagnose the effect of soil water availability on O_3 risk by assuming soil water at field capacity (FC), i.e., $f_{soil} = 1$ at every timestep. These runs are named "FC-runs", as opposed to the rainfed runs (Table 1).

UKESM1-0-LL simulates O_3 concentrations reasonably accurately, whereas GFDL-ESM4 underestimates upper O_3 concentration percentiles (see Appendix SA.2). For this reason, data from UKESM1-0-LL is used for all four runs, while GFDL-ESM4 data from the historical experiment is only used for the MM + CO_2 run.

Each run produces global annual POD_6 maps from 2000 to 2099 for each of the considered SSP. All maps and tables in this study are masked with the land-use maps from Qiao et al. (2023). Furthermore, for a given year, we excluded any grid node where wheat fails to reach maturity before the next prescribed sowing date. O_3 concentration and f_{clim} values (Section 3.1) are surveyed by computing the global mean and the mean of the interannual variability. First, in every node, the mean yearly value of each

TABLE 1 | List of acronyms and symbols and their meaning.

Acronym/ symbol	Meaning
ANOVA	Analysis of variance
CL	Critical level
EP	Emission policy
ESM	Earth system model
FC	Field capacity
f_{clim}	Jarvis function defined as
f_{CO_2}	Jarvis function for CO_2
f_{light}	Jarvis function for light
f_{min}	Jarvis function to indicate the minimum gs expressed relative to the gsmax
f_{O_3}	Jarvis function for the O_3-induced senescence
f_{phen}	Jarvis function for phenological growth
F_{sO_3}	O_3 stomatal flux
f_{soil}	Jarvis function for soil water availability to the plant
f_{temp}	Jarvis function for temperature
f_{VPD}	Jarvis function for VPD
g_s	Stomatal conductance to O_3
$g_{s,max}$	Maximum of stomatal conductance
I	Interaction factor between EP and RF in the ANOVA
MM	Mapping manual (LRTAP Convention 2017)
PLA	Projected leaf area
POD_Y	Phytotoxic ozone dose above a threshold of Y nmol $m^{-2} s^{-1}$ PLA
R_a	Atmospheric resistance
R_b	Quasi-laminar sublayer resistance
R_c	Surface resitance
R_{cut}	Cuticular resitance
RF	Radiative Forcing
R_{inc}	Intra-canopy resistance
R_{soil}	Soil resistance
R_{stom}	Stomatal resistance
RYL	Relative yield loss
TOAR	Tropospheric ozone assessment report

variable is calculated, over the daylight hours of the accumulation period. Then, for that node, yearly values over a given time window (2000–2014, 2045–2054, or 2090–2099) are considered, and the mean and the standard deviation are calculated using those values. The final mean values (Table 2) are obtained by averaging all the mean values in every node (global mean). The global interannual variability is calculated from the mean of the standard deviations obtained in every node (spatial mean of the interannual variability). The analysis of regional trends in Section 3.2 is restricted to the *area at O_3 risk*, i.e., the nodes that exceed the CL for wheat (1.3 mmol m^{-2} PLA) for at least 1 year of the century under any SSP. This restriction allows us to focus on the parts of the regions where O_3 risk is non-negligible at any point in time, excluding consistently low-POD_6 areas. For each region, it is tested whether the mean POD_6 value over a selected future time window significantly differs from the mean POD_6 value at the baseline (Welch t-test, with efficient sample size calculated for spatial autocorrelation calculated using Moran's Index). The *p*-values are computed by comparing the 15 annual means of the baseline period over a certain region with the 10 annual means in each future time window (Table 3 and Table S3). In Section 3.3, we define a grid node as *chronically at risk* under a given experiment if POD_6 exceeds the CL in at least 75% of the years considered (either 2000–2014 or 2015–2099). This criterion identifies areas where O_3 risk is persistent across the century, even when end-century POD_6 declines. This definition allows to assess whether an area of the globe is at O_3 risk throughout the century, even with decreasing POD_6 end-century values. We also estimate global production losses at the baseline, at 2050 and at 2100. We use gridded annual yield output (Tg $yr.^{-1}$) from the LPJmL model (Lutz et al. 2019; Von Bloh et al. 2018), as per simulations performed within ISIMIP3b (Jägermeyr et al. 2024) using UKESM1-0-LL as climate forcing dataset. This product offers gridded annual yield values (t ha^{-1}) at global-scale for the historical, SSP1-2.6, SSP3-7.0 and SSP5-8.5 experiments. We combine these yield data with the harvested area from the Spatial Production Allocation Model (SPAM2020v2) dataset of the International Food Policy Research Institute (International Food Policy Research Institute (IFPRI) 2024) to calculate the total wheat production in each grid node. By combining these products with the estimated RYL (Equation (5)), we then obtain the annual production losses (Tg $yr.^{-1}$) under both present and future climate scenarios. Therefore, this approach captures projected yield changes across different SSPs but assumes that the spatial distribution of wheat cultivation remains fixed at present-day levels as defined by SPAM.

3 | Results

3.1 | Spatio-Temporal Patterns of O_3 and Impacts of Climate Variables on Stomatal Conductance

Figure 1a–d shows the mean O_3 concentrations during the *baseline* years (2000–2014 mean) and their changes (ΔO_3) at 2100 (2090–2099 mean). O_3 concentrations are expressed at wheat canopy height and averaged over the daylight hours of the accumulation period. During the baseline years, UKESM1-0-LL shows global mean O_3 concentrations of 37.1 ± 2.4 ppb (Table 2), while GFDL-ESM4 shows slightly lower values (36.0 ± 2.1 ppb). The Northern Hemisphere presents higher O_3 concentrations than the Southern Hemisphere, with the Middle East and Asia as the regions with the highest values around the globe (Figure 1a). Compared to GFDL-ESM4, UKESM1-0-LL shows stronger latitudinal and elevation gradients (see Figure S2 for GFDL-ESM4

TABLE 2 | Global means (±mean interannual variability) of O_3 concentrations at canopy height, Jarvis functions, and duration of the accumulation period during the baseline period, at 2050 and 2100, and differences in the onsets of the accumulation periods between the end of the century and the baseline (Δonset), over wheat-growing regions, for UKESM1-0-LL under the different SSPs.

		2050[a]			2100[a]		
Variable	**Baseline[a]**	**SSP1-2.6**	**SSP3-7.0**	**SSP5-8.5**	**SSP1-2.6**	**SSP3-7.0**	**SSP5-8.5**
O_3 [ppb]	37.1 ± 2.4	32.6 ± 2.1	38.9 ± 2.3	40.2 ± 2.4	28.6 ± 1.8	39.5 ± 2.4	37.7 ± 2.5
f_{clim} [0,1]	0.34 ± 0.07	0.35 ± 0.07	0.38 ± 0.07	0.36 ± 0.08	0.36 ± 0.07	0.39 ± 0.08	0.36 ± 0.08
f_{temp} [0,1]	0.60 ± 0.06	0.69 ± 0.05	0.68 ± 0.06	0.72 ± 0.05	0.7 ± 0.05	0.69 ± 0.06	0.72 ± 0.05
f_{VPD} [0,1]	0.89 ± 0.04	0.84 ± 0.05	0.86 ± 0.05	0.82 ± 0.05	0.84 ± 0.04	0.83 ± 0.05	0.77 ± 0.06
f_{soil} [0,1]	0.66 ± 0.08	0.61 ± 0.09	0.68 ± 0.08	0.61 ± 0.09	0.61 ± 0.09	0.71 ± 0.08	0.66 ± 0.08
Accumulation period duration [days]	40.6 ± 10.9	41.0 ± 8.8	38.1 ± 9.6	39.6 ± 8.2	40.9 ± 8.8	32.6 ± 9.3	37.1 ± 9.4
Δonset [days]		−0.1 ± 5.9	−2.2 ± 5.3	−4.3 ± 5.8	−3.5 ± 5.9	−12.6 ± 4.4	−23.4 ± 5.3

[a]Baseline indicates the mean between 2000 and 2014, 2050 indicates the mean between 2045 and 2054, and 2100 indicates the mean between 2090 and 2099.

TABLE 3 | Mean POD_6 (mmol m^{-2} PLA) for the MM run by region and SSP for areas at risk at the *baseline* (2000–2014) at *2050* (2045–2054) and *2100* (2090–2099).

	Baseline POD_6 [mmol m^{-2}]	**2050 POD_6 [mmol m^{-2}]**			**2100 POD_6 [mmol m^{-2}]**		
Region[a]	**Historical**	**SSP1-2.6**	**SSP3-7.0**	**SSP5-8.5**	**SSP1-2.6**	**SSP3-7.0**	**SSP5-8.5**
East Asia	1.65 ± 1.47	**0.95 ± 1.00**	**1.97 ± 1.62**	**1.98 ± 1.67**	**0.37 ± 0.40**	1.71 ± 1.39	**1.00 ± 0.93**
South-East Asia	1.01 ± 1.21	0.83 ± 1.06	**1.36 ± 1.51**	**1.30 ± 1.64**	**0.40 ± 0.73**	**1.49 ± 1.68**	**0.68 ± 1.01**
South Asia	0.81 ± 1.43	0.75 ± 1.45	**1.52 ± 2.18**	**1.23 ± 2.14**	**0.41 ± 0.91**	**1.69 ± 2.22**	0.82 ± 1.50
Central Asia	0.34 ± 0.39	**0.17 ± 0.29**	**0.75 ± 0.73**	**0.49 ± 0.62**	**0.09 ± 0.15**	**0.77 ± 0.66**	0.33 ± 0.33
North America	1.59 ± 1.00	**0.30 ± 0.30**	**0.90 ± 0.60**	**0.99 ± 0.77**	**0.18 ± 0.21**	**0.61 ± 0.43**	**0.84 ± 0.67**
Central America	0.50 ± 0.75	**0.26 ± 0.69**	0.58 ± 0.98	**0.80 ± 1.23**	**0.11 ± 0.36**	**0.71 ± 1.04**	**0.32 ± 0.61**
South America	0.63 ± 0.85	**0.24 ± 0.27**	**0.87 ± 0.70**	**0.81 ± 0.70**	**0.13 ± 0.21**	**0.92 ± 0.69**	**0.34 ± 0.42**
Russia–Belarus–Ukraine	0.77 ± 0.49	**0.18 ± 0.23**	**0.66 ± 0.49**	**0.55 ± 0.45**	**0.09 ± 0.13**	**0.59 ± 0.44**	**0.53 ± 0.41**
Europe	1.03 ± 0.89	**0.27 ± 0.35**	1.04 ± 0.80	**0.90 ± 0.86**	**0.15 ± 0.21**	1.03 ± 0.73	0.99 ± 0.79
North Africa	0.64 ± 0.67	**0.18 ± 0.26**	0.72 ± 0.74	**0.46 ± 0.60**	**0.10 ± 0.20**	0.54 ± 0.68	**0.25 ± 0.49**
Sub-Saharan Africa	0.49 ± 0.60	0.44 ± 0.53	**0.71 ± 0.75**	**0.99 ± 0.98**	**0.21 ± 0.34**	**0.98 ± 1.15**	**0.76 ± 1.02**
Middle East	0.18 ± 0.42	**0.11 ± 0.29**	**0.38 ± 0.69**	0.21 ± 0.55	**0.03 ± 0.09**	**0.64 ± 0.82**	**0.26 ± 0.42**

Note: Bold values indicate that the $p < 0.05$. See Table S3 for actual p-values and for the 95% confidence intervals for the difference in means reported in this table.
[a]Region definitions are based on those established by the Hemispheric Transport of Air Pollutants (HTAP2; Huang et al. 2017).

2000–2014 maps) and generally reports higher concentrations at latitudes <45°, except for the Eastern Indian peninsula. Moreover, UKESM1-0-LL simulates the strongest seasonal cycle in Northern Hemisphere surface ozone among all CMIP6 models, potentially due to excessive NO_x titration of O_3 in this model (Turnock et al. 2020). Under SSP1-2.6, which assumes the implementation of strong air quality policies, UKESM1-0-LL projects a mean O_3 decrease of 8.5 ppb by the end of the century (Figure 1b). On the contrary, under SSP3-7.0, which is characterized by weaker air pollution control policies, O_3 concentrations generally increase by 2100, although some exceptions are present (e.g., central U.S.; Figure 1c). SSP5-8.5 shows similar spatial patterns as SSP3-7.0, but to a lesser extent, which is consistent with the implementation of strong air quality control policies from 2050 onward (Figure 1d).

The f_{clim} function captures the combined effect of key climatic factors (air temperature, VPD and soil water available to the plant) on g_s. Values of $f_{clim} \approx 1$ indicate minimal limitation, while near zero values denote a strong stomatal closure and reduced O_3 uptake. During the baseline years, the f_{clim} averaged over the accumulation period exceeds 0.5 over large areas of Eastern North America, South America, and East Asia, while strongly limiting conditions ($f_{clim} < 0.2$) occur mostly in arid

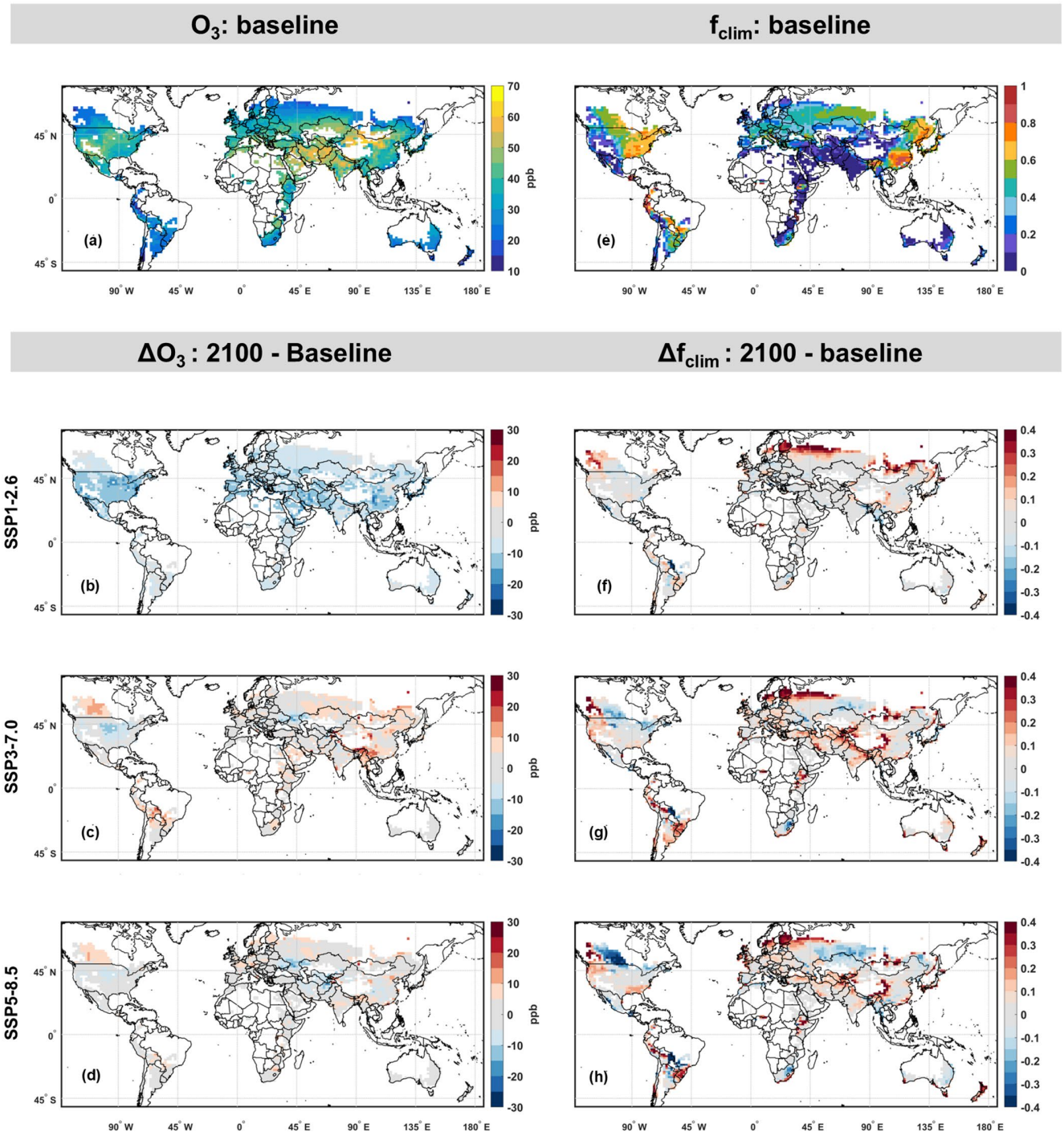

FIGURE 1 | Ozone mean concentrations at canopy height and during the daylight hours of the accumulation period for UKESM1-0-LL over the baseline period (a), and ΔO_3 at 2100 with respect to the baseline across the different SSPs (b–d). f_{clim} mean values for the same ESM over the baseline period (e), and Δf_{clim} at 2100 with respect to the baseline across the different SSPs (f–h). $f_{clim} = f_{temp} \cdot f_{VPD} \cdot f_{soil}$ summarizes the limitations to g_s due to temperature, VPD and soil water available to the plant, with values ranging from 0 to 1 depending on whether they are limiting or not. Positive or negative Δf_{clim} correspond to higher and lower O_3 risk, respectively (red and blue, in f–h). Baseline indicates the 2000–2014 mean, and 2100 indicates the 2090–2099 mean. White nodes indicate that wheat either is not grown or hasn't reached maturity before the next prescribed sowing date (see Section 2.3). This assumption applies to all the figures presented hereafter. Map lines delineate study areas and do not necessarily depict accepted national boundaries.

regions (Figure 1e). Figure 1f–h shows the changes in f_{clim} at 2100 compared to the baseline (Δf_{clim}). From an O_3 risk perspective, negative Δf_{clim} values indicate stronger climatic limitation of g_s and thus, potentially, lower POD_6 and O_3 damage. On the contrary, positive Δf_{clim} values correspond to a weaker limitation of g_s and therefore higher POD_6 and increased O_3 damage. SSP3-7.0 and SSP5-8.5 indicate overall similar magnitudes of Δf_{clim} across the globe at the end of the century, while SSP1-2.6 shows smaller changes, as expected from the weaker RF of this scenario. An evident pattern in future changes across all SSPs

is the large positive shift at latitudes >45°, which indicates higher g_s (and better growing conditions) for wheat at higher latitude. This is due to increased f_{temp} values, i.e., temperatures closer to the optimum for g_s (Figure S3a–d). The function f_{VPD} (Figure S3e–h) is generally non-limiting ($f_{VPD} > 0.8$) across most regions of the globe, with the only exception of arid regions, indicating that f_{clim} is only marginally affected by this component. However, f_{VPD} becomes more limiting at the end of the century because of a general decrease in relative humidity, which is a feature frequently observed in future climate simulations (e.g., Fang et al. 2022). As expected, f_{soil} is very limiting over arid regions at the present time, but increases considerably at the end of the century under SSP3-7.0 and SSP5-8.5 (Figure S3i–l). Overall, during the baseline, f_{clim} is primarily constrained by f_{soil} (see e.g., Figure 1e and Figure S3i). However, the positive changes in f_{clim} at 2100 appear to be driven by the changes in f_{temp} at higher latitudes and in f_{soil} over arid regions, but this effect is counteracted by the negative changes in f_{VPD}, especially under SSP3-7.0 and SSP5-8.5.

Finally, it is important to highlight that the POD_6 accumulation period becomes slightly shorter and noticeably earlier in the future (Table 2), especially under SSP3-7.0 and SSP5-8.5, and therefore the O_3 concentrations and the outcomes of the Jarvis functions described in this section are affected by this time shift.

3.2 | POD_6 Trends by Region

Figure 2 displays the annual POD_6 values averaged over different geographical regions and under different SSPs, for both the MM and MM + CO_2 runs. Table 3 lists the mean POD_6 at *2050* (2045–2054) and at *2100* (2090–2099) in each region (p-values and 95% confidence intervals are reported in Table S3). POD_6 decreases under SSP1-2.6 in every region for both the MM and the MM + CO_2 runs, with values reaching approaching zero well before 2100. These results are associated with very high certainty ($p < 0.001$) in most regions at the end of the century. For the MM run, POD_6 generally does not decrease under SSP3-7.0, with 7 out of 12 regions displaying increasing POD_6 values at the end of the century ($p < 0.01$). For the same run, under SSP5-8.5, POD_6 changes at 2050 are associated with $p < 0.01$ in 6 regions, and in these cases the timelines rise and then fall, usually reaching their maxima between 2050 and 2080, and then reverting to values closer or lower than of the baseline at the end of the century. In the MM + CO_2 run POD_6 values decrease in every region, as the limiting effect of increasing CO_2 on g_s dominates the other dynamics (O_3 concentrations and f_{clim} changes). This is especially evident in the differences between MM and MM + CO_2 end-century POD_6 values for SSP5-8.5, which are very large precisely due to the high CO_2 concentrations under this scenario. As this feature is consistent across regions and quite straightforward, it will not be commented further, and the rest of this section will refer only to the MM run.

Noticeably, East Asia is the region with the largest area at O_3 risk and with the highest average POD_6 values at both the baseline (1.65 ± 0.17 mmol m^{-2}) and across all scenarios, exceeding the CL for the whole century under SSP3-7.0, and for most of it under SSP5-8.5. South Asia has the second greatest POD_6 value across all SSPs (1.07) over a fairly large O_3 risk area, experiencing the largest absolute POD_6 increase under SSP3-7.0 at both 2050 and 2100 (+0.71 and + 0.88 respectively). In this region, the average POD_6 frequently exceeds the CL under both SSP3-7.0 and SSP5-8.5. South-East Asia has the third highest POD_6 average across all SSPs (1.01), although the hotspot region is comparatively small. This region shows highest variability in POD_6 values, with an interannual standard deviation across SSPs of 0.41 mmol m^{-2}, most likely reflecting the largest interannual variability of O_3 concentrations and f_{clim} among all regions (interannual SD: 4.77 ppb and 0.08, respectively). Sub-Saharan Africa is another region with a large POD_6 increase across SSPs (+0.19), which corresponds to POD_6 values doubling at mid-century under SSP5-8.5 and at the end of the century under SSP3-7.0. In Europe the average POD_6 values over areas at O_3 risk are typically just below the CL, and they do not show any detectable change at the end of the century under SSP3-7.0 and SSP5-8.5. Even so, this O_3 risk area covers 79.9% of Europe and, across the century, 28.2% of the times the CL is exceeded anyway. Furthermore, it should be noticed that the close to zero changes in POD_6 values are due to the presence of opposing trends between Southern and Northern Europe (see Figure 3), rather than due to an actual absence of changes in POD_6 mean values. North America has the second highest average POD_6 at the baseline over a widespread O_3 risk area, but POD_6 values most certainly decrease across all the scenarios (−0.95, $p < 0.001$) and for future times the mean POD_6 would exceed the CL only under SSP5-8.5 and for just a few years. Russia–Belarus–Ukraine also shows decreasing POD_6 values under any scenario ($p < 0.001$), and while the O_3 risk is quite extended, the CL is seldomly exceeded over individual nodes and years.

3.3 | Global Estimates of POD_6 and Agronomic Losses

Figure 3 shows POD_6 global maps for the baseline period and at the end of the century. In this figure, the POD_6 values refer to the two contrasting assumptions on the effect of CO_2 concentrations on g_s (MM and MM + CO_2 runs). During the baseline years, the mean POD_6 exceeds the CL for wheat over the 17.5% and 16.1% of the global wheat area in the MM and MM + CO_2 runs, respectively (Figure 3a), leading to global production losses of 28.7 and 26.6 Tg $yr.^{-1}$ respectively (Table S4). An important indicator to identify hotspots is the percentage of years during which the POD_6 surpasses the CL across the whole century (Figure 4). Figure 4a shows this indicator at the baseline, during which 11.7% of the nodes can be classified as chronically at risk in the MM run (10.0% in the MM + CO_2 run).

Under SSP1-2.6, O_3 risk decreases across the whole globe by the end of the century (Figure 3b,c), mostly due to declining O_3 concentrations (Figure 1b), with the mean POD_6 above the CL for only the 0.8% and 0.5% of the global wheat area, in the MM and MM + CO_2 runs respectively (% areas chronically at risk: 0.6% and 0.2%; production losses: 5.7 and 3.9 Tg $yr.^{-1}$). Such decrease is consistent almost everywhere also for SSP3-7.0 and SSP5-8.5 in the case of the MM + CO_2 run (Figure 3e,g), due to the limiting effect on g_s of the increasing CO_2 concentrations. On the other hand, changes in the MM run are not as straightforward (Figure 3d,f), indicating major spatial discrepancies across regions. In any case, globally, the mean POD_6 at the end

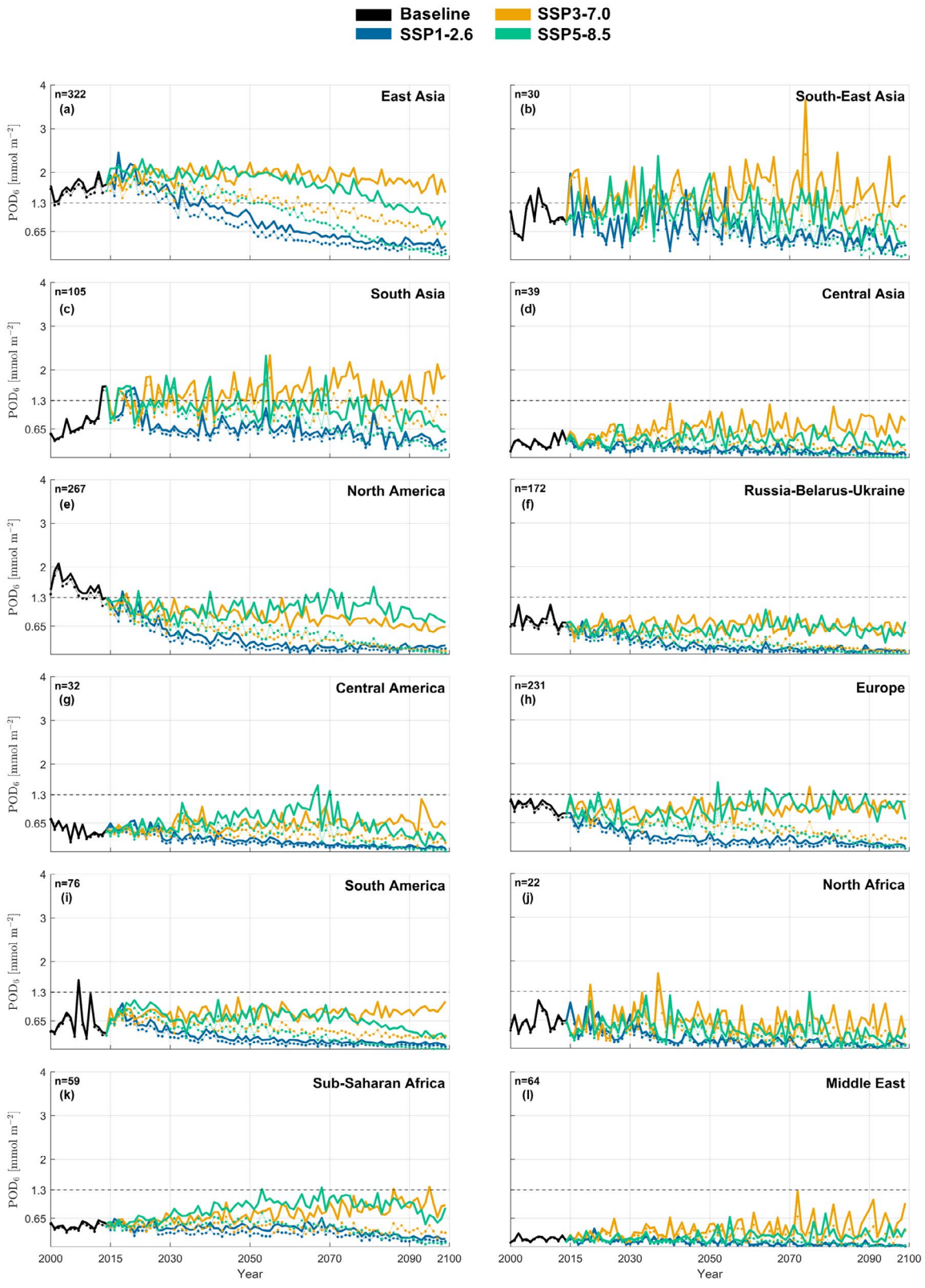

FIGURE 2 | POD_6 throughout the century with respect to the baseline average, shown across different SSPs and divided by region, for both the MM run (solid lines) and the MM + CO_2 run (dotted lines); only the areas at O_3 risk within each region are considered. The value (*n*) in the upper-left corner is the number of nodes in the areas at O_3 risk. The dashed horizontal line corresponds to the CL for wheat.

of the century exceeds the CL over smaller areas, compared to the baseline. In fact, this area amounts to 14.5% (−3.0%) and to 10.8% (−5.3%) at the end of the century in the MM run, for SSP3-7.0 and SSP5-8.5 respectively (% areas chronically at risk: 9.3% and 5.8%; production losses: 33.3 and 23.4 Tgyr.$^{-1}$). For the MM + CO_2 run, these areas are even smaller (% domain above CL on average: 3.5% and 0.3%; % areas chronically at risk: 2.0% and 0.3%; production losses: 12.3 and 3.5 Tgyr.$^{-1}$). Since this run

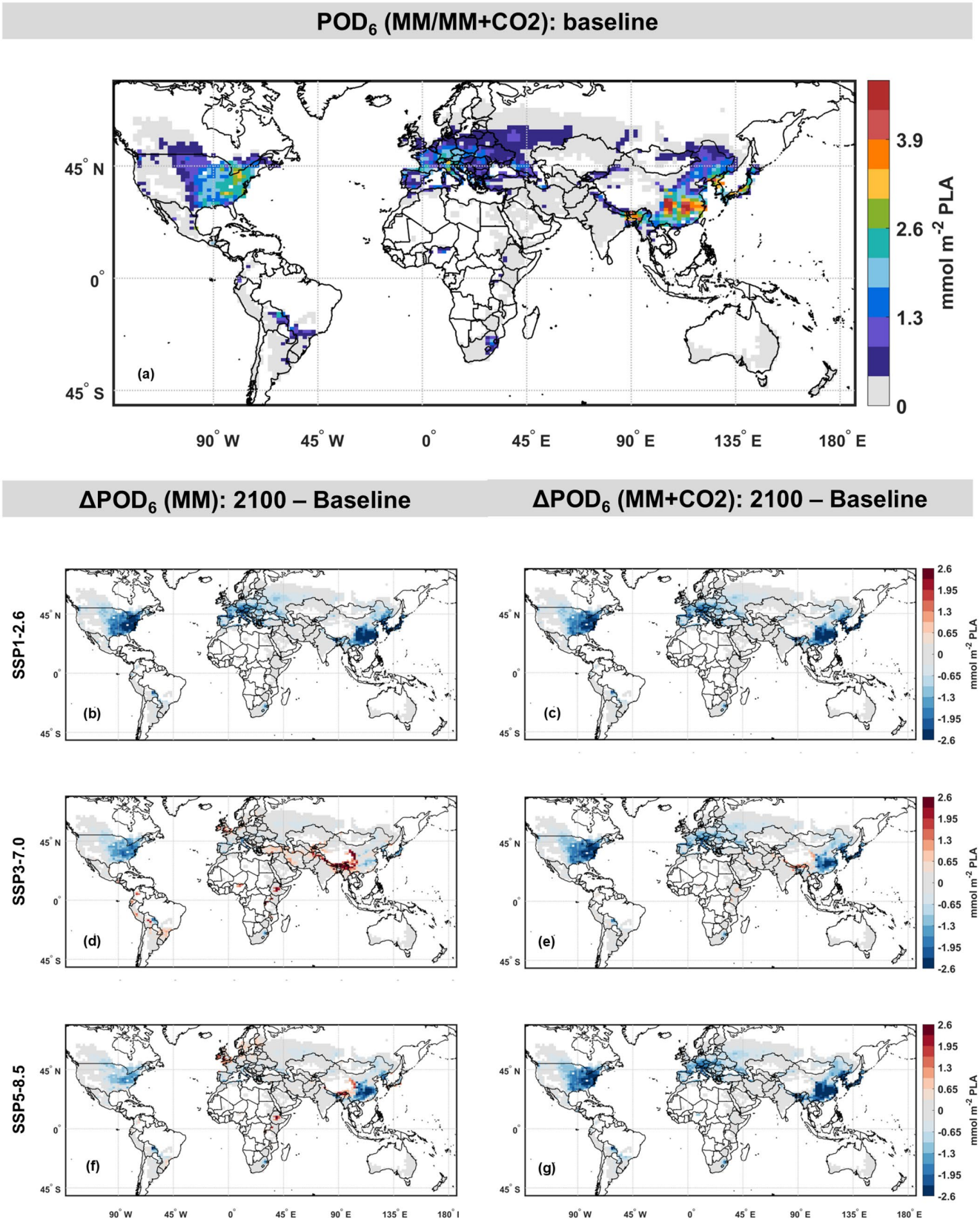

FIGURE 3 | Mean POD_6 over the baseline period (a), and ΔPOD_6 at 2100 with respect to the baseline across the different SSPs for the MM run (b,d,f) and the MM + CO_2 run (c,e,g). For the baseline only one map is shown, as the differences between the two runs are barely noticeable. Note: Baseline indicates the mean between 2000 and 2014, and 2100 indicates the mean between 2090 and 2099. Map lines delineate study areas and do not necessarily depict accepted national boundaries.

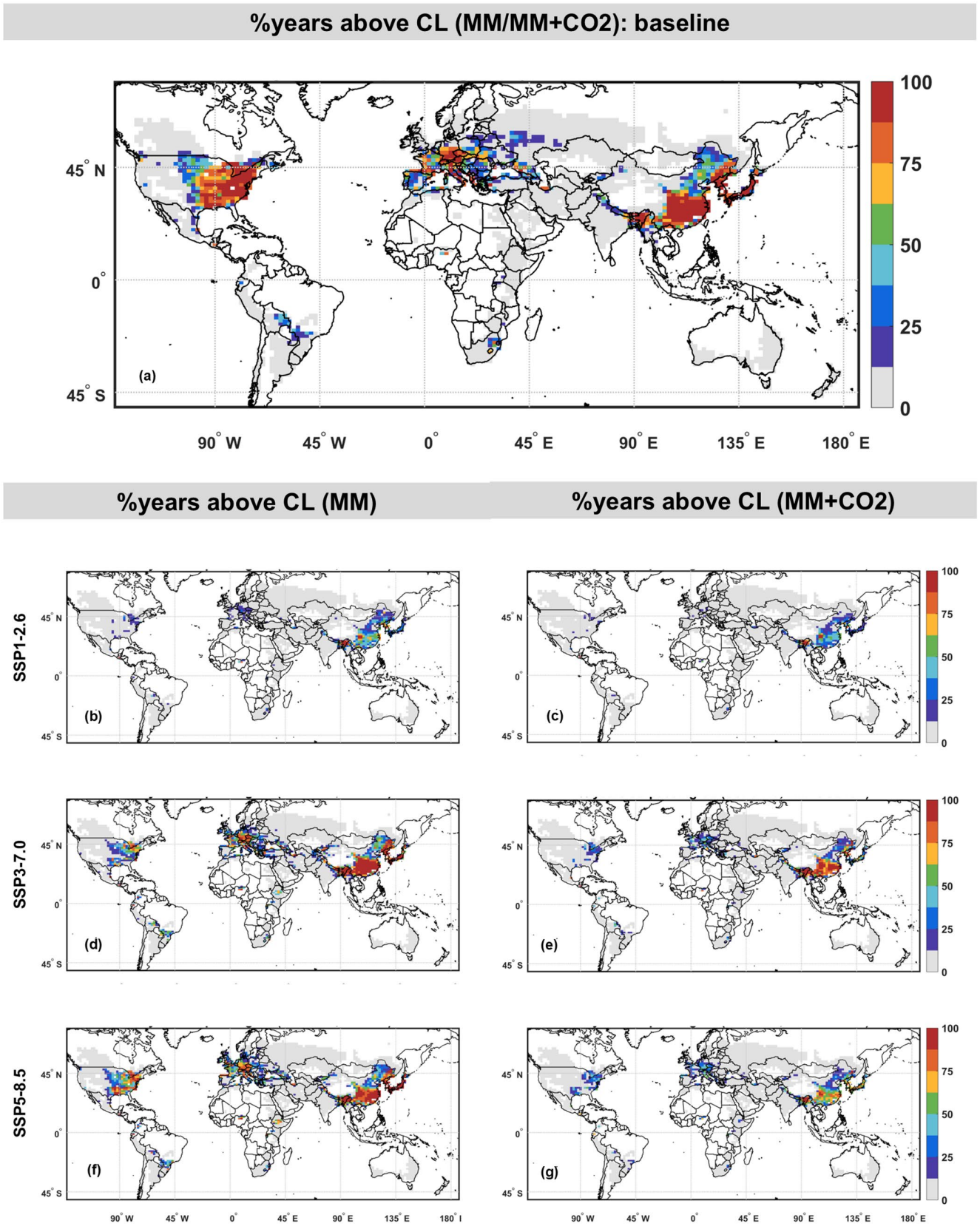

FIGURE 4 | Percentage of years exceeding the CL for wheat (1.3 mmol m^{-2}), at the baseline (a) and under different SSPs (b–g), in the MM run (b,d,f) and in the MM + CO_2 run (c,e,g). Reference periods cover the whole experiments, i.e., for the baseline is 2000–2014, and for the SSPs is 2015–2099. Map lines delineate study areas and do not necessarily depict accepted national boundaries.

predicts a general decrease almost everywhere, no region-by-region investigation is needed.

For the MM run, the three regions with the highest POD_6 values at the baseline (East Asia, North America, Europe) follow different trends and dynamics in the remaining part of the century. In East Asia, POD_6 changes are more complex under SSP3-7.0 and SSP5-8.5, as they appear to be negative or fairly constant in the eastern part of the region (Eastern China, Korea, Japan), but positive closer to the Tibetan plateau (Yunnan, Sichuan, and Gansu provinces of China). Regardless of these end-of-century decreases, some areas of chronic risk persist across the century under every SSP. Eastern North America is the only region with an evident decrease in O_3 risk under any scenario, which is due to the decreasing O_3 concentrations (Figure 1b) in a fairly constant f_{clim} (Figure 1f). This is also reflected in the shrinking of the areas chronically at risk across all scenarios (Figure 4d,f). In Europe, O_3 risk hotspots shift from Southern to Northern Europe, following less limiting temperatures for stomatal O_3 uptake at high latitudes (Figure S2c,d), and a slightly more limiting soil water availability to wheat in the southern part of the region (Figure S2k,l). Future chronic risk appears to persist mostly over Central Europe. The MM run identifies the largest increased risk in the southern and eastern edges of the Tibetan plateau (from Kashmir to the Gansu province) by the end of the century, an area that is included within South, South-East and East Asia, in the present region classification (Huang et al. 2017). Within this region, Nepal, Bhutan, and East India reach the mean POD_6 peak value of 8.6 mmol m^{-2} PLA for SSP3-7.0 and 6.6 mmol m^{-2} PLA for SSP5-8.5 at 2100. This area is chronically at O_3 risk under any scenario, not only for the MM run, but also for the MM + CO_2 run. Other areas with increased O_3 risk are also present within Sub-Saharan Africa, Central and South America, especially under scenario SSP3-7.0.

Using the Equation (5), the POD_6 in Figure 3 can be converted to RYL. In this regard, the highest RYL values achieved across the region can be defined as the 95th percentile over the areas at risk. On the basis of the POD_6 values calculated in the MM run, the highest RYL values over East Asia are around 17.2% at the present time (mean RYL: 6.4%), with no relevant changes at the end of the century under SSP3-7.0 (95th perc.: 16.7%; mean: 6.6%). Under SSP5-8.5 and SSP1-2.6 these peak values decrease to 10.5% and 4.6% (mean: 3.9% and 1.4%) respectively, by the end of the century. In South Asia, the present-day highest RYL values are above 15.7% (mean: 3.1%), and increase to become the highest worldwide under SSP3-7.0 (95th perc.: 25.3%; mean: 6.5%). Under SSP5-8.5, the increase in RYL is small (95th perc.: 17.1%; mean: 3.2%), while under SSP1-2.6 the highest RYL values considerably decrease to around 9.6%. Nonetheless, this value is the highest across the globe for this scenario and well above the CL for wheat. In Europe, the highest RYL values are estimated to be around 9.4%–10.3% (mean: 3.8%–4.0%), at the beginning and at the end of the century under SSP3-7.0 and SSP5-8.5. On the other hand, under SSP1-2.6, the 95th percentile of RYL is substantially lower (2.3%). In North America, the highest RYL values at the baseline are 13.1% (mean: 6.1%), and decrease under every scenario, although some areas still experience relevant damage under SSP3-7.0 and SSP5-8.5 (95th perc.: 5.4% and 8.1%; mean: 2.3% and 3.2%). From the present day to the end of the century, the highest RYL values in South-East Asia increase from 12.9% to 18.7% under SSP3-7.0 (mean: from 3.9% to 5.7%), in Sub-Saharan Africa from 6.4% to 12.2% and 11.8% under SSP3-7.0 and SSP5-8.5 (mean: from 1.9% to 3.8% and 2.9%), and in Central America from 7.7% to 12.1% under SSP3-7.0 (mean: from 1.9% to 2.7%).

Figure S3f shows the POD_6 over the baseline calculated with the GFDL-ESM4, for the MM + CO_2 run. As expected, given that the O_3 concentrations are largely underestimated in the upper percentiles, the POD_6 values are much lower compared to the UKESM1-0-LL results. For this ESM, only a few areas appear to have relevant O_3 damage, but it should be noted that they correspond to the three regions that were also highlighted in the UKESM1-0-LL case (Eastern North America, Europe, East Asia).

Figure S4 shows the differences between POD_6 calculated with the FC runs and POD_6 calculated with the rainfed runs. Differences in POD_6 are reported for the baseline and for the end of the century and across SSPs. As expected, baseline differences between the FC runs and the rainfed runs vary spatially, mostly in line with soil water availability limitations to wheat (Figure S3i). For future times, when the CO_2 effect on g_s is excluded, the spatial pattern of the differences remains similar to the baseline, although with different magnitudes (Figure S4, left column). In this case, the areas at O_3 risk expand by +65.1%, with the average POD_6 increasing by +0.53 mmol m^{-2}. On the other hand, when the CO_2 effect is included, the process is largely dominated by the limiting effects of rising CO_2, and the differences between FC and rainfed runs become minimal (Figure S4, right column). In the MM_FC run, South-East Asia is the region with the largest increase in POD_6 over O_3 risk areas under all SSPs, relatively to the MM run. This is true at both mid and end century, with differences reaching up to 2.4 mmol m^{-2} under SSP3-7.0 and SSP5-8.5 at 2050. Sub-Saharan Africa and Central America O_3 risk areas expand more than twice, with differences as large as 1.15 mmol m^{-2}. In Sub-Saharan Africa the largest differences are located in the region between Kenya and Tanzania, and, unlike the MM run, the average POD_6 value across O_3 risk area exceeds the CL at the baseline, for all SSPs at 2050, and for SSP3-7.0 at 2100. In South Asia the most pronounced differences occur mostly in the first half of the century, with a +59% expansion of the O_3 risk areas. In Europe, the largest differences in POD_6 values between the MM_FC and MM runs are located in the southern part of the region, with increases of $+0.50 \pm 0.17$ mmol m^{-2} across scenarios.

3.4 | Drivers of POD_6 Changes

Here we perform a two-way ANOVA (see details in Appendix SA.6) on the MM run results to assess which factor among EP, RF, and their interaction (I) has the most significant influence on POD_6 changes at the end of the century around the globe. The specific levels of EP and RF associated with each SSP are described in Table A4. Figure 5a shows for each grid node the factor with the most certain effect (i.e., the lowest *p*-value among the ones smaller than 0.05) as identified by the two-way ANOVA, while Figure 5b–d display the total variance explained by each factor (R^2), allowing further quantification of their contributions to POD_6 changes. *p*-values maps for each factor considered in the ANOVA are shown in Figure S6. The ANOVA reveals different geographical patterns where the POD_6 changes are mostly driven by the

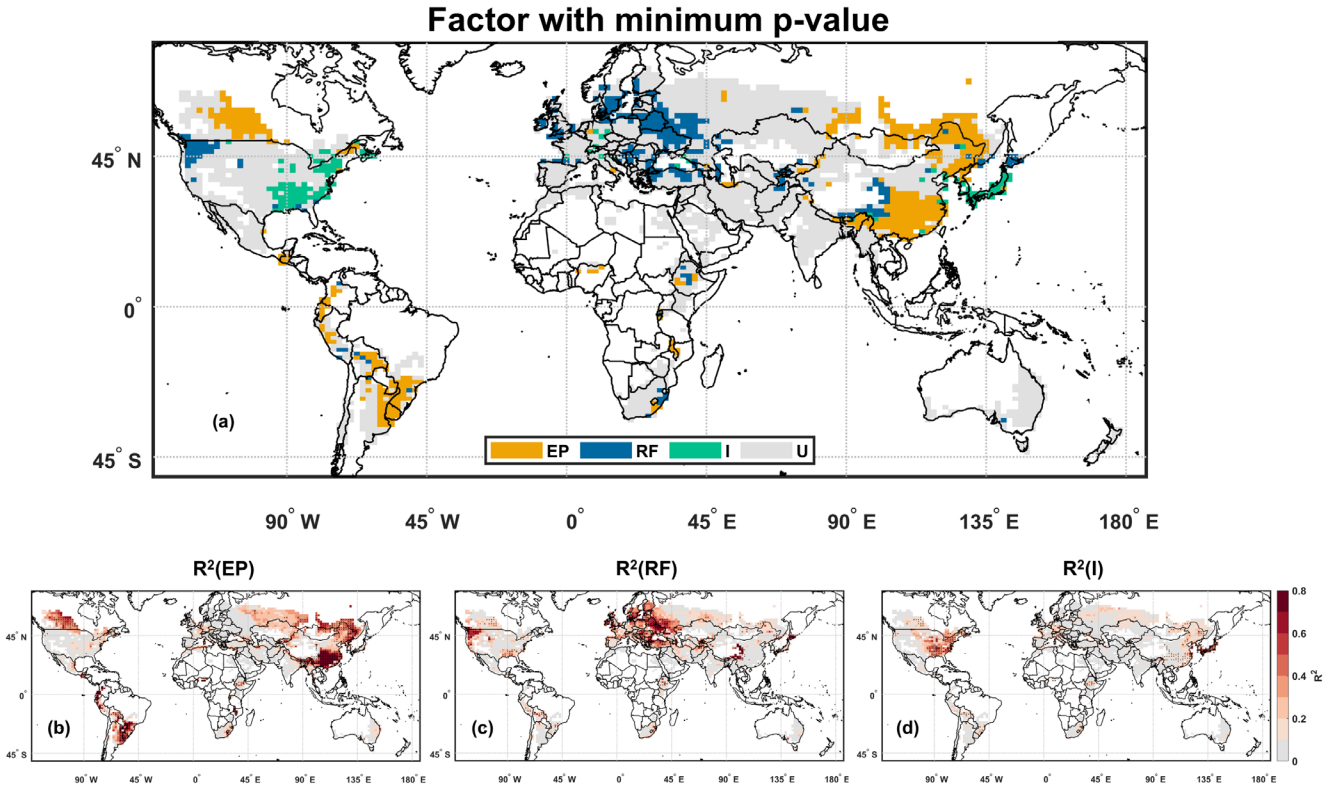

FIGURE 5 | Map of the factors with the most certain (minimum p-value, among factors with $p < 0.05$, corrected with Bonferroni) impact on POD_6 changes at the end of the century, identified by the two-way ANOVA (a). Explained variance R^2 associated with each factor in each node, with black dots indicating p-value < 0.05 (b–d). See Figure S6 for maps of the p-values for each factor included in the ANOVA. EP = Emission Policy, RF = Radiative Forcing, I = Interaction, U = Uncertain (i.e., $p > 0.05$ for all factors). Map lines delineate study areas and do not necessarily depict accepted national boundaries.

same factor. For example, in East China the decrease of POD_6 under SSP1-2.6 and SSP5-8.5 (Figure 2; Figure 3; Table 3) most certainly depends on EP. Similarly, in South America POD_6 changes are controlled by EP. In the eastern U.S. and in Japan the large decrease in POD_6 under all SSPs (Figure 3) is controlled by the interaction between EP and RF. In Russia–Belarus–Ukraine and in Northern Europe (lat. > 45°) changes in POD_6 are clearly driven by RF, and this is mostly due to the increasing temperatures lifting the f_{temp} limitations at higher latitudes in future times (Figure S3). These findings suggest that in regions where RF is the dominant driver, POD_6 may increase even under strong EP. In regions where POD_6 decreases the ANOVA identifies the factors that are mainly responsible for this decrease, such as in East China, Eastern U.S. and Japan. In contrast, where POD_6 increases the ANOVA indicates which policies could be more effective to mitigate O_3 risk for crops. For instance, in Northern Europe, where RF is responsible for the POD_6 increase, the adoption of stricter reduction policies on greenhouse gases emissions at a global level, rather than only the adoption of local EP, would lead to reduction of O_3 risk for crops as a climate co-benefit.

At the global scale, we identify the variables most closely associated with relevant POD_6 changes, depending on the considered SSP. Table S4 shows the mean 2000–2014 values of several variables (O_3 concentration, f_{clim}, f_{temp}, f_{VPD}, f_{soil}, and duration of the accumulation period) over the areas where a factor was identified by the ANOVA (i.e., the areas marked as EP, RF or I, but not as U). The table also shows the mean changes (±SD) in these variables across the nodes and years with large POD_6 changes (i.e., below −0.65 or above +0.65 mmol m^{-2}) for each SSP. The larger negative changes in POD_6 are found under SSP1-2.6 and are mainly due to a strong decrease in O_3 concentrations (−10.2 ± 4.6 ppb). Under SSP3-7.0 and SSP5-8.5, POD_6 reductions are instead mainly associated with a decrease in f_{clim} (−0.08 ± 0.15 and −0.07 ± 0.18, respectively). In particular, this decrease is the largest in the VPD component under these two scenarios (−0.06 ± 0.11 and −0.11 ± 0.14). On the other hand, large increases in POD_6 rarely occur under SSP1-2.6 (0.1% of all the considered nodes) and they seem to be driven by a marked increase in f_{clim} (+0.25 ± 0.13). For SSP3-7.0 and SSP5-8.5, the increases in POD_6 result from a combination of rising O_3 concentrations (7.6 ± 7.1 and 3.3 ± 5.4 ppb) and f_{clim} values (0.19 ± 0.13 and 0.25 ± 0.14). In these scenarios, the largest contribution to f_{clim} is from reduced temperature limitations, with f_{temp} increasing by 0.16 ± 0.15 and 0.25 ± 0.18 for SSP3-7.0 and SSP5-8.5, respectively.

4 | Discussion

4.1 | Future O_3 Risk for Wheat and Implications for Food Security

This study shows how future O_3 levels and climatic conditions may impact wheat production across different areas of the globe and highlights how varying assumptions can lead

to contrasting results in terms of risk estimates. The MM run follows the common approach for O_3 risk assessment and, while being considered suitable for the present time, it does not account for the limiting effect that increasing atmospheric CO_2 may exert on g_s. Conversely, the MM + CO_2 run, which includes CO_2-induced stomatal limitations, projects substantial decreases in future POD_6 values. However, even when considering the CO_2-driven decrease in POD_6 values at the end of the century, there are parts of the globe that remain chronically at risk throughout the century. The FC runs (MM_FC and MM + CO_2_FC) provide stricto sensu an estimate of the maximum potential damage under no limitation to soil water availability to the plants. These runs could also be interpreted as representing the O_3 risk under optimal irrigation, and could better represent the damage over arid areas, which rely on irrigation for wheat cultivation.

Our results can provide insights into potential consequences for global food security in the broader context of the SSPs. Under SSP1-2.6, a consistent and very certain decline in O_3 risk is observed across all regions and model configurations. This decrease is mostly driven by global reductions in O_3 concentrations, implying minimal impacts on wheat productivity at the end of the century. In fact, the annual global production losses under this scenario range from 3.9 to 11.5 Tg yr.$^{-1}$ (depending on the run considered), which corresponds to 0.5%–1.4% of the total wheat production, while during the baseline production losses are in the range of 26.6–40.1 Tg yr.$^{-1}$ (3.3%–5.0%). Reduced production losses would promote food sovereignty, thus easing climate adaptation challenges. In contrast, under SSP3-7.0, O_3 risk persists throughout the century, increasing in several world regions such as Asia, South America, and Sub-Saharan Africa, although some of the projected damage may be mitigated by the CO_2 limiting effect on g_s (annual global production losses: 12.3–44.8 Tg yr.$^{-1}$, 1.3%–4.9%). In this scenario, O_3 risk is driven not only by increased precursor emissions, but also by climate-induced enhancement of O_3 uptake, indicating that precursors control alone may be insufficient to reduce significantly O_3 damage, especially over the regions where POD_6 changes are controlled by RF (Section 3.4). Moreover, given SSP3's assumptions of restricted international cooperation and trade, the resulting food security threats would be further exacerbated. SSP5-8.5 represents an intermediate case: O_3 risk increases until around 2050 in many regions (up to 19.7–44.0 Tg yr.$^{-1}$, 2.2%–5.0%) and then declines to baseline or lower values by the end of the century (3.5–30.9 Tg yr.$^{-1}$, 0.5%–2.6%). This trend reflects the implementation of mid-century air quality policies explicitly assumed by this scenario (Kriegler et al. 2017). The POD_6 increase is mainly driven by climate forcing, but the extremely high CO_2 levels at the end of the century under this scenario, may likely alleviate O_3 damage globally via stomatal limitation. In addition, this scenario envisions strong technological advancement, potentially enabling effective adaptations to emerging food security risks.

O_3 risk hotspots should also be discussed, alongside policies that could potentially reduce the risk in these regions. The Southern and Eastern edges of the Tibetan Plateau (i.e., parts of East and South Asia) show consistent O_3 risk through the century, even when the CO_2 limiting effect on g_s is considered. Here, POD_6 values will remain high even under the MM + CO_2 run, indicating that this region will likely represent a persistent O_3 hotspot throughout the 21st century. This vulnerability may result from the combined effects of stratospheric O_3 transport across this region (Yin et al. 2023) and less limitations to g_s in future climate (Figure 1). In this area, mitigation of O_3 risk would likely require joint reductions in both O_3 precursors and greenhouse gases emissions. More broadly, South Asia also emerges as a critical region, not only near the Tibetan Plateau, but also across the many other parts of the region that have a widespread need for irrigation (Brauman et al. 2013; Chiarelli et al. 2020). Over this area, O_3 risk is observed in the FC runs, which might provide a better estimate of POD_6 changes. Given the agricultural importance of the Indian peninsula and the Tibetan Plateau for global wheat productions (Monfreda et al. 2008), these regions should be considered at the highest O_3 risk across the 21st century. East Asia is also identified as a high-risk area in the MM run. POD_6 values are projected to decrease under SSP1-2.6 and SSP5-8.5, but not under SSP3-7.0, indicating the effectiveness of O_3 precursor control policies. In fact, under SSP3-7.0, POD_6 values increase substantially, although this projection might be exaggerated, as O_3 precursor emissions in China have already decreased significantly since 2014 (Van Der et al. 2017). Beyond these primary risk regions, increases in POD_6, particularly in Central America, South America, and Sub-Saharan Africa, are relatively large compared to the baseline and could grow larger under the FC assumptions (Figure S4). This is particularly concerning for Sub-Saharan Africa, where high population growth and developmental challenges are expected throughout the 21st century (Kc and Lutz 2017; United Nations Department of Economic and Social Affairs, Population Division 2022). Nevertheless, our results suggest that strong precursors emission controls could have a key role in reducing O_3 risk in this region. On the other hand, Eastern U.S., which is currently among the most critical regions for wheat O_3 damage is projected to experience a reduction in POD_6 values under all SSPs, likely due to combined controls on both O_3 precursors and greenhouse gases emissions. In Northern Europe instead, O_3 risk appears to be primarily driven by climate change, suggesting that global efforts in mitigating greenhouse gas emissions may be the viable strategy to reduce O_3 impacts in the region.

4.2 | Uncertainty Sources in O_3 Risk Projections

One of the main sources of uncertainty in this study concerns the extent to which rising atmospheric CO_2 concentrations reduce g_s in wheat. Current knowledge on this effect remains limited and uncertain, as experimental data show high variability due to methodological differences (e.g., presence or absence of acclimatation to elevated CO_2 during plant growth), species-specific physiological traits, and diverse environmental conditions during the experiments. Furthermore, unavoidable uncertainties arise from possible future developments in crop breeding, such as for instance, plant breeding selection for new varieties with higher g_s to enhance photosynthesis, or the emergence of epigenetic responses to prolonged high-CO_2 exposure. These factors make it difficult to accurately predict the magnitude of g_s reductions and their implications for future POD_6 estimates.

A second source of uncertainty relates to the phenological-stage modeling of wheat. Our simulations adopt the accumulated thermal time to determine the beginning and end of the POD accumulation period, following the approach prescribed by the MM (LRTAP Convention 2017). As shown in Appendix SA.5, this method produces globally reasonable estimates of crop maturity dates (Figure A3). However, regional discrepancies can arise (Figure A4), introducing additional uncertainty into the POD_6 estimations at the local scale.

Another important source of uncertainty arises from the feedback between O_3 damage and vegetation physiology, which is not accounted for in this study. Specifically, O_3-induced damage may reduce stomatal O_3 uptake by vegetation, thereby increasing atmospheric O_3 concentrations and reinforcing O_3 uptake in other regions, while also influencing local climate conditions (Emberson et al. 2013). The Earth System Models from CMIP6 considered in this study do not include vegetation-O_3 feedbacks, and as a result, may underestimate these dynamics. Capturing this mechanism, would require rerunning the ESM simulations with an explicit representation of O_3 effects on vegetation. This approach would enable one to jointly account for this specific feedback and for all the other processes that influence O_3 dynamics in the atmosphere (photochemistry), which are already included in CMIP6 models with coupled-chemistry schemes (including GFDL-ESM4 and UKESM1-0-LL).

Our analysis suggests that the uncertainty in the input ESM variables has a modest impact on the results of this study (Appendix SA.2). The coarser spatio-temporal resolution from the CMIP6 models can lead to underestimation of O_3 flux peaks (Guaita et al. 2023) and to misrepresentations of local meteorological features influenced by topography and land cover (Brands 2022). Furthermore, all CMIP6 models were found to overestimate mean surface O_3 concentrations in the 2005–2014 period when compared to observations, with biases reaching up to 16 ppb in some regions (Turnock et al. 2020). However, O_3 concentrations are known to be lower near the ground surface (Gerosa et al. 2017), while the vertical resolution of CMIP6 models places the first atmospheric layer at 14–20 m above ground. As a consequence, O_3 concentration absolute bias (Appendix SA.2) is much smaller when modeled O_3 concentrations are scaled to measurement height. This evaluation also shows that peak O_3 values are simulated accurately for UKESM1-0-LL after scaling. The effect of the input variables (meteorology and O_3 concentrations) on the final POD_6 estimate is calculated for UKESM1-0-LL (Equation SA2), and our results show that the uncertainty propagates to the POD_6 estimates mostly through the variability component only, rather than on the bias.

4.3 | Comparison With Previous O_3 Risk Assessments for Wheat

Previous studies, although based on different modeling approaches and typically limited to present-day conditions, generally show good agreement with our findings in terms of spatial patterns and hotspots of O_3 damage (Lombardozzi et al. 2015; Schauberger et al. 2019; Sitch et al. 2007; Tai et al. 2021). Specifically, these studies identified the eastern U.S., Europe, and East Asia as critical regions for O_3-related crop damage, showing substantial spatial agreement with our results. Mills et al. (2018) provided a global-scale estimate of O_3 risk for wheat using the POD_3IAM metric for the years 2010–2012, within a modeling framework similar to ours. They also identified the same major hotspots but reported higher relative yield losses and production impacts. Specifically, their study estimated average global production losses of approximately 85.0 Tg $yr.^{-1}$, whereas our baseline period estimates are considerably lower (28.7–39.9 Tg $yr.^{-1}$). This discrepancy is unlikely to result from differences in model input data or parameterizations, but rather from the different O_3 risk metric employed in their study. In fact, POD_6 has a higher O_3 detoxification threshold, such that null yield losses may occur even when the corresponding POD_3IAM values are greater than zero. Consequently, the RYL calculated via POD_6 could be zero, even when the RYL calculated via POD_3IAM is not, and the production losses calculated with POD_3IAM are expected to be systematically higher, especially in regions where O_3 stomatal fluxes consistently remain lower than 6 but above 3 nmol O_3 m^{-2} s^{-1}.

Some differences emerge when comparing our findings to regional assessments of present-day O_3 impacts on wheat. For example, POD_6 was estimated to reach values up to 8.5 mmol m^{-2} in the Iberian Peninsula (De Andrés et al. 2012), while our results indicate some potential threats without reaching such extreme POD_6 values. On the other hand, our findings are consistent with recent estimates of POD_3IAM in Sub-Saharan Africa under the FC assumption (Sharps, Vieno, et al. 2021), and with studies identifying O_3-affected areas in China (Cao et al. 2024; Wang et al. 2023; Wang et al. 2022).

Li et al. (2025) calculated O_3-related production losses to wheat over China for both present (2015–2019) and future times (2056–2060, under SSP1-2.6, SSP3-7.0 and SSP5-8.5), using the Jarvis model to calculate POD_{12} at a 36×36 km resolution. Consistently with the other regional-scale studies, they reported much larger present-day O_3 impacts, compared to our results (production losses amounting to 26 Tg $yr.^{-1}$, vs. ours 9.9–11.1 Tg $yr.^{-1}$). As their modeling framework is akin to ours, the different magnitude most likely stems from the much finer spatial resolution used in their study and, possibly, from the different input data, g_s parameterizations, and detoxification threshold for POD ($Y = 12$). Similarly to us, they concluded that, under SSP1-2.6, the O_3 damage significantly decreases at future times and identified reductions in O_3 precursors emission as the main driver of this trend. Furthermore, they found relevant O_3 damage increases under SSP3-7.0. This result is consistent with our MM run, but not with the MM + CO_2 run. As Li et al. (2025) did not include any CO_2-induced reduction on g_s, this discrepancy is an indication that accounting for CO_2 limitations to g_s constitutes a key feature for estimating O_3 risk at future times.

Few studies have estimated O_3 effects on wheat under future climate change scenarios, while explicitly accounting for the CO_2-induced limitation of g_s. One of the most recent examples is provided by Zhou et al. (2024), who used the ModelE2-YIBs model to simulate the effects of O_3 on gross primary

productivity (GPP) in 2010 and 2060 under SSP1-2.6 and SSP5-8.5. Despite some minor regional differences, particularly in Western Africa and South America likely due to their broader focus on vegetation rather than wheat, their spatial patterns of O_3 risk closely resemble ours. However, the relatively coarse spatial resolution used in their study (2°×2.5°) may limit the ability to resolve finer-scale risk patterns captured in our simulations. Klingberg et al. (2011) also explored future POD changes at 10 European sites, accounting for the effect of rising CO_2 on stomatal O_3 uptake. Their findings, like ours, showed that even under pessimistic greenhouse gas scenarios, future stomatal uptake of O_3 would remain constant or decrease due to CO_2-induced reductions in g_s. Similarly to our approach, they implemented an explicit CO_2-limiting function (f_{CO_2}) that linearly reduced g_s by 34% between 360 and 560 ppm, with no further decrease beyond this range. While this assumption is biologically reasonable within that interval, a linear extrapolation beyond 560 ppm could yield implausibly low g_s values, potentially approaching zero at very high CO_2 levels. In our case, the f_{CO_2} function is more conservative: we estimate an 18% reduction in g_s between 360 and 560 ppm, with the function extending to higher CO_2 concentrations while avoiding biologically unrealistic values. Under SSP5-8.5, for instance, f_{CO_2} implies a total g_s reduction of 47.2% from 360 ppm to the end-century CO_2 level of 1067 ppm. Zhou et al. (2024) also accounted for the CO_2 effect, though implicitly, through the use of a Ball–Berry-type stomatal conductance model that links g_s to net photosynthesis. While our approach is more explicitly formulated, the parameterization of the f_{CO_2} we apply is derived from Ball–Berry–Farquhar simulations, and thus we would not expect major discrepancies in the CO_2-limiting effect between our work and theirs.

5 | Conclusions

This study quantified the global and regional evolution of O_3 risk to wheat under three SSPs up to 2100 and explored alternative assumptions about the CO_2 limiting effect on g_s and about water availability to the plant. Our results indicate that, at the global scale, O_3 risk is expected to decline by the end of the century, although transient risks may persist in the near future. Even without any assumed CO_2-g_s interaction, the O_3 damage is generally projected to decrease. However, there may be persistent O_3 damage hotspots across several regions, with the extent and intensity of the risk strongly depending on the scenario considered. When the effect of elevated CO_2 on g_s is considered, the O_3 risk is projected to decline to near-zero values across most regions under all SSPs.

Nevertheless, substantial uncertainties remain regarding the limiting effect of elevated CO_2 concentrations on g_s. Moreover, the present modeling framework does not account for any vegetation feedback to O_3 concentrations and climate. For these reasons, the large projected decrease in POD_6 under CO_2-limiting scenarios may be exaggerated, and a more realistic future O_3 risk probably lies between the outcomes of simulations with and without the CO_2 effect. Consequently, future studies on O_3 risk assessments should aim to reduce these uncertainties. Research efforts should focus on experimental assessments and validation of the physiological interaction between elevated CO_2 and O_3 uptake under field conditions, and their combined effects on stomatal conductance and carbon assimilation.

Author Contributions

Pierluigi R. Guaita: conceptualization, data curation, formal analysis, investigation, methodology, software, validation, visualization, writing – original draft, writing – review and editing. **Riccardo Marzuoli:** funding acquisition, methodology, resources, supervision, writing – original draft, writing – review and editing. **Leiming Zhang:** writing – original draft, writing – review and editing. **Steven Turnock:** investigation, writing – original draft, writing – review and editing. **Gerbrand Koren:** writing – review and editing. **Oliver Wild:** writing – original draft, writing – review and editing. **Paola Crippa:** methodology, supervision, writing – original draft, writing – review and editing. **Giacomo Gerosa:** conceptualization, funding acquisition, methodology, project administration, resources, software, supervision, writing – original draft, writing – review and editing.

Acknowledgments

We thank Dr. Shengchao Qiao and colleagues for their valuable contribution in providing the sowing dates dataset of wheat and for their useful comments to adapt their results to our case study. This manuscript benefits from discussions during the meeting of the Ozone Deposition Focus working group of the Tropospheric Ozone Assessment Report, phase II.

Funding

This work was supported by the FUTUROZ Project of the national "5x1000 funding to research" (Ministry of University and Research), by Catholic University of the Sacred Heart in the frame of its Programs of promotion and dissemination of the scientific research [Funding line D3.1], and by the U.S. National Science Foundation under Grant No. 2347239 to PC.

Conflicts of Interest

The authors declare no conflicts of interest.

Data Availability Statement

Output from GFDL-ESM4 and UKESM1-0-LL simulations is publicly available from the ESGF metagrid site (Cinquini et al. 2014). The data for individual years used to produce the figures in this study is publicly available at https://doi.org/10.5281/zenodo.17501006. The underlying Matlab code is available at https://github.com/prguaita/O3-Deposition-model-for-wheat. The full documentation of the model is available in Guaita et al. (2023).

References

Agrawal, M., and S. S. Deepak. 2003. "Physiological and Biochemical Responses of Two Cultivars of Wheat to Elevated Levels of CO_2 and SO_2, Singly and in Combination." *Environmental Pollution* 121, no. 2: 189–197. https://doi.org/10.1016/S0269-7491(02)00222-1.

Ainsworth, E. A., and A. Rogers. 2007. "The Response of Photosynthesis and Stomatal Conductance to Rising [CO_2]: Mechanisms and Environmental Interactions." *Plant, Cell & Environment* 30, no. 3: 258–270. https://doi.org/10.1111/j.1365-3040.2007.01641.x.

Ainsworth, E. A., C. R. Yendrek, S. Sitch, W. J. Collins, and L. D. Emberson. 2012. "The Effects of Tropospheric Ozone on Net Primary Productivity and Implications for Climate Change." *Annual Review of Plant Biology* 63, no. 1: 637–661. https://doi.org/10.1146/annurev-arplant-042110-103829.

Anav, A., A. De Marco, C. Proietti, et al. 2016. "Comparing Concentration-Based (AOT40) and Stomatal Uptake (PODY) Metrics for Ozone Risk Assessment to European Forests." *Global Change Biology* 22, no. 4: 1608–1627. https://doi.org/10.1111/gcb.13138.

Anav, A., L. Menut, D. Khvorostyanov, and N. Viovy. 2011. "Impact of Tropospheric Ozone on the Euro-Mediterranean Vegetation." *Global Change Biology* 17, no. 7: 2342–2359. https://doi.org/10.1111/j.1365-2486.2010.02387.x.

Baldocchi, D. D., B. B. Hicks, and P. Camara. 1987. "A Canopy Stomatal Resistance Model for Gaseous Deposition to Vegetated Surfaces." *Atmospheric Environment (1967)* 21, no. 1: 91–101. https://doi.org/10.1016/0004-6981(87)90274-5.

Ball, J. T., I. E. Woodrow, and J. A. Berry. 1987. "A Model Predicting Stomatal Conductance and Its Contribution to the Control of Photosynthesis Under Different Environmental Conditions." In *Progress in Photosynthesis Research*, edited by J. Biggens, vol. 4, 221–224. Martinus Nijhoff Publishers. https://doi.org/10.1007/978-94-017-0519-6_48.

Brands, S. 2022. "A Circulation-Based Performance Atlas of the CMIP5 and 6 Models for Regional Climate Studies in the Northern Hemisphere Mid-To-High Latitudes." *Geoscientific Model Development* 15, no. 4: 1375–1411. https://doi.org/10.5194/gmd-15-1375-2022.

Brauman, K. A., S. Siebert, and J. A. Foley. 2013. "Improvements in Crop Water Productivity Increase Water Sustainability and Food Security—A Global Analysis." *Environmental Research Letters* 8, no. 2: 24030. https://doi.org/10.1088/1748-9326/8/2/024030.

Cao, J., X. Yue, and M. Ma. 2024. "Simulation of Ozone–Vegetation Coupling and Feedback in China Using Multiple Ozone Damage Schemes." *Atmospheric Chemistry and Physics* 24, no. 7: 3973–3987. https://doi.org/10.5194/acp-24-3973-2024.

Charusombat, U., D. Niyogi, A. Kumar, et al. 2010. "Evaluating a New Deposition Velocity Module in the Noah Land-Surface Model." *Boundary-Layer Meteorology* 137, no. 2: 271–290. https://doi.org/10.1007/s10546-010-9531-y.

Cheesman, A. W., F. Brown, M. N. Farha, et al. 2023. "Impacts of Ground-Level Ozone on Sugarcane Production." *Science of the Total Environment* 904: 166817. https://doi.org/10.1016/j.scitotenv.2023.166817.

Chiarelli, D. D., C. Passera, L. Rosa, K. F. Davis, P. D'Odorico, and M. C. Rulli. 2020. "The Green and Blue Crop Water Requirement WATNEEDS Model and Its Global Gridded Outputs." *Scientific Data* 7, no. 1: 273. https://doi.org/10.1038/s41597-020-00612-0.

Chuwah, C., T. Van Noije, D. P. Van Vuuren, E. Stehfest, and W. Hazeleger. 2015. "Global Impacts of Surface Ozone Changes on Crop Yields and Land Use." *Atmospheric Environment* 106: 11–23. https://doi.org/10.1016/j.atmosenv.2015.01.062.

Cinquini, L., D. Crichton, C. Mattmann, et al. 2014. "The Earth System Grid Federation: An Open Infrastructure for Access to Distributed Geospatial Data." *Future Generation Computer Systems* 36: 400–417. https://doi.org/10.1016/j.future.2013.07.002.

Clifton, O. E., D. Schwede, C. Hogrefe, et al. 2023. "A Single-Point Modeling Approach for the Intercomparison and Evaluation of Ozone Dry Deposition Across Chemical Transport Models (Activity 2 of AQMEII4)." *Atmospheric Chemistry and Physics* 23, no. 17: 9911–9961. https://doi.org/10.5194/acp-23-9911-2023.

Collins, W. J., J.-F. Lamarque, M. Schulz, et al. 2017. "AerChemMIP: Quantifying the Effects of Chemistry and Aerosols in CMIP6." *Geoscientific Model Development* 10, no. 2: 585–607. https://doi.org/10.5194/gmd-10-585-2017.

De Andrés, J. M., R. Borge, D. De La Paz, J. Lumbreras, and E. Rodríguez. 2012. "Implementation of a Module for Risk of Ozone Impacts Assessment to Vegetation in the Integrated Assessment Modelling System for the Iberian Peninsula. Evaluation for Wheat and Holm Oak." *Environmental Pollution* 165: 25–37. https://doi.org/10.1016/j.envpol.2012.01.048.

Del Pozo, A., P. Pérez, R. Morcuende, A. Alonso, and R. Martínez-Carrasco. 2005. "Acclimatory Responses of Stomatal Conductance and Photosynthesis to Elevated CO_2 and Temperature in Wheat Crops Grown at Varying Levels of N Supply in a Mediterranean Environment." *Plant Science* 169, no. 5: 908–916. https://doi.org/10.1016/j.plantsci.2005.06.009.

Dunne, J. P., L. W. Horowitz, A. J. Adcroft, et al. 2020. "The GFDL Earth System Model Version 4.1 (GFDL-ESM 4.1): Overall Coupled Model Description and Simulation Characteristics." *Journal of Advances in Modeling Earth Systems* 12, no. 11: e2019MS002015. https://doi.org/10.1029/2019MS002015.

Emberson, L. 2020. "Effects of Ozone on Agriculture, Forests and Grasslands." *Philosophical Transactions of the Royal Society A: Mathematical, Physical and Engineering Sciences* 378, no. 2183: 20190327. https://doi.org/10.1098/rsta.2019.0327.

Emberson, L. D., M. R. Ashmore, H. M. Cambridge, and D. Simpson. 2000. "Modelling Stomatal Ozone Flux Across Europe." *Environmental Pollution* 109: 403–413.

Emberson, L. D., N. Kitwiroon, S. Beevers, P. Büker, and S. Cinderby. 2013. "Scorched Earth: How Will Changes in the Strength of the Vegetation Sink to Ozone Deposition Affect Human Health and Ecosystems?" *Atmospheric Chemistry and Physics* 13, no. 14: 6741–6755. https://doi.org/10.5194/acp-13-6741-2013.

Emberson, L. D., D. Simpson, J.-P. Tuovinen, M. R. Ashmore, and H. M. Cambridge. 2000. "Towards a Model of Ozone Deposition and Stomatal Uptake Over Europe." EMEP/MSC-W Note 6/2000. DET NORSKE METEOROLOGISKE INSTITUTT.

Eyring, V., S. Bony, G. A. Meehl, et al. 2016. "Overview of the Coupled Model Intercomparison Project Phase 6 (CMIP6) Experimental Design and Organization." *Geoscientific Model Development* 9, no. 5: 1937–1958. https://doi.org/10.5194/gmd-9-1937-2016.

Fang, Z., W. Zhang, M. Brandt, A. M. Abdi, and R. Fensholt. 2022. "Globally Increasing Atmospheric Aridity Over the 21st Century." *Earth's Future* 10, no. 10: e2022EF003019. https://doi.org/10.1029/2022EF003019.

Farquhar, G. D., S. Von Caemmerer, and J. A. Berry. 1980. "A Biochemical Model of Photosynthetic CO_2 Assimilation in Leaves of C3 Species." *Planta* 149, no. 1: 78–90. https://doi.org/10.1007/BF00386231.

Fischer, M. L., D. P. Billesbach, J. A. Berry, W. J. Riley, and M. S. Torn. 2007. "Spatiotemporal Variations in Growing Season Exchanges of CO_2, H_2O, and Sensible Heat in Agricultural Fields of the Southern Great Plains." *Earth Interactions* 11, no. 17: 1–21. https://doi.org/10.1175/EI231.1.

Fiscus, E. L., F. L. Booker, and K. O. Burkey. 2005. "Crop Responses to Ozone: Uptake, Modes of Action, Carbon Assimilation and Partitioning." *Plant, Cell & Environment* 28, no. 8: 997–1011. https://doi.org/10.1111/j.1365-3040.2005.01349.x.

Franks, P. J., J. A. Berry, D. L. Lombardozzi, and G. B. Bonan. 2017. "Stomatal Function Across Temporal and Spatial Scales: Deep-Time Trends, Land-Atmosphere Coupling and Global Models." *Plant Physiology* 174, no. 2: 583–602. https://doi.org/10.1104/pp.17.00287.

Fuhrer, J., M. Val Martin, G. Mills, et al. 2016. "Current and Future Ozone Risks to Global Terrestrial Biodiversity and Ecosystem Processes." *Ecology and Evolution* 6, no. 24: 8785–8799. https://doi.org/10.1002/ece3.2568.

Fujimori, S., T. Hasegawa, T. Masui, et al. 2017. "SSP3: AIM Implementation of Shared Socioeconomic Pathways." *Global Environmental Change* 42: 268–283. https://doi.org/10.1016/j.gloenvcha.2016.06.009.

Gerosa, G., S. Cieslik, and A. Ballarin-Denti. 2003. "Micrometeorological Determination of Time-Integrated Stomatal Ozone Fluxes Over Wheat:

A Case Study in Northern Italy." *Atmospheric Environment* 37, no. 6: 777–788. https://doi.org/10.1016/S1352-2310(02)00927-5.

Gerosa, G., R. Marzuoli, B. Monteleone, M. Chiesa, and A. Finco. 2017. "Vertical Ozone Gradients Above Forests. Comparison of Different Calculation Options With Direct Ozone Measurements Above a Mature Forest and Consequences for Ozone Risk Assessment." *Forests* 8, no. 9: 337. https://doi.org/10.3390/f8090337.

González-Fernández, I., V. Bermejo, S. Elvira, et al. 2013. "Modelling Ozone Stomatal Flux of Wheat Under Mediterranean Conditions." *Atmospheric Environment* 67: 149–160. https://doi.org/10.1016/j.atmosenv.2012.10.043.

Grulke, N. E., and R. L. Heath. 2020. "Ozone Effects on Plants in Natural Ecosystems." *Plant Biology* 22, no. S1: 12–37. https://doi.org/10.1111/plb.12971.

Grünhage, L., H. Pleijel, G. Mills, et al. 2012. "Updated Stomatal Flux and Flux-Effect Models for Wheat for Quantifying Effects of Ozone on Grain Yield, Grain Mass and Protein Yield." *Environmental Pollution* 165: 147–157. https://doi.org/10.1016/j.envpol.2012.02.026.

Guaita, P. R., R. Marzuoli, and G. A. Gerosa. 2023. "A Regional Scale Flux-Based O3 Risk Assessment for Winter Wheat in Northern Italy, and Effects of Different Spatio-Temporal Resolutions." *Environmental Pollution* 333: 121860. https://doi.org/10.1016/j.envpol.2023.121860.

Haworth, M., D. Killi, A. Materassi, A. Raschi, and M. Centritto. 2016. "Impaired Stomatal Control Is Associated With Reduced Photosynthetic Physiology in Crop Species Grown at Elevated [CO_2]." *Frontiers in Plant Science* 7: 1568. https://doi.org/10.3389/fpls.2016.01568.

Horowitz, L. W., V. Naik, L. Sentman, et al. 2018. "*NOAA-GFDL GFDL-ESM4 Model Output Prepared for CMIP6 AerChemMIP* (Version 20230720) [Application/x-Netcdf]." Earth System Grid Federation. https://doi.org/10.22033/ESGF/CMIP6.1404.

Hoshika, Y., E. Paoletti, E. Agathokleous, T. Sugai, and T. Koike. 2020. "Developing Ozone Risk Assessment for Larch Species." *Frontiers in Forests and Global Change* 3: 45. https://doi.org/10.3389/ffgc.2020.00045.

Huang, M., G. R. Carmichael, R. B. Pierce, et al. 2017. "Impact of Intercontinental Pollution Transport on North American Ozone Air Pollution: An HTAP Phase 2 Multi-Model Study." *Atmospheric Chemistry and Physics* 17, no. 9: 5721–5750. https://doi.org/10.5194/acp-17-5721-2017.

International Food Policy Research Institute (IFPRI). 2024. "Global Spatially-Disaggregated Crop Production Statistics Data for 2020 Version 2.0 (Version 4.0) [Dataset]." Harvard Dataverse. https://doi.org/10.7910/DVN/SWPENT.

Jägermeyr, J., C. Müller, S. Minoli, D. Ray, and S. Siebert. 2021. "*GGCMI Phase 3 Crop Calendar* [Dataset]." Zenodo. https://doi.org/10.5281/ZENODO.5062513.

Jägermeyr, J., S. Rabin, J. Balkovic, et al. 2024. "*ISIMIP3b Simulation Data from the Agriculture Sector* (Version 1.2) [Dataset]." ISIMIP Repository. https://doi.org/10.48364/ISIMIP.723340.2.

Jarvis, P. G. 1976. "The Interpretation of the Variations in Leaf Water Potential and Stomatal Conductance Found in Canopies in the Field." *Philosophical Transactions of the Royal Society of London. B, Biological Sciences* 273, no. 927: 593–610. https://doi.org/10.1098/rstb.1976.0035.

Kang, H., T. Zhu, Y. Zhang, et al. 2021. "Elevated CO_2 Enhances Dynamic Photosynthesis in Rice and Wheat." *Frontiers in Plant Science* 12: 727374. https://doi.org/10.3389/fpls.2021.727374.

Karlsson, P. E., S. Braun, M. Broadmeadow, et al. 2007. "Risk Assessments for Forest Trees: The Performance of the Ozone Flux Versus the AOT Concepts." *Environmental Pollution* 146, no. 3: 608–616. https://doi.org/10.1016/j.envpol.2006.06.012.

Kc, S., and W. Lutz. 2017. "The Human Core of the Shared Socioeconomic Pathways: Population Scenarios by Age, Sex and Level of Education for All Countries to 2100." *Global Environmental Change* 42: 181–192. https://doi.org/10.1016/j.gloenvcha.2014.06.004.

Klingberg, J., M. Engardt, P. E. Karlsson, J. Langner, and H. Pleijel. 2014. "Declining Ozone Exposure of European Vegetation Under Climate Change and Reduced Precursor Emissions." *Biogeosciences* 11, no. 19: 5269–5283. https://doi.org/10.5194/bg-11-5269-2014.

Klingberg, J., M. Engardt, J. Uddling, P. E. Karlsson, and H. Pleijel. 2011. "Ozone Risk for Vegetation in the Future Climate of Europe Based on Stomatal Ozone Uptake Calculations." *Tellus A: Dynamic Meteorology and Oceanography* 63, no. 1: 174. https://doi.org/10.1111/j.1600-0870.2010.00465.x.

Krasting, J. P., J. G. John, C. Blanton, et al. 2018. *NOAA-GFDL GFDL-ESM4 Model Output Prepared for CMIP6 CMIP historical* (Version 20230220) [Application/x-netcdf] Earth System Grid Federation. https://doi.org/10.22033/ESGF/CMIP6.8597.

Kriegler, E., N. Bauer, A. Popp, et al. 2017. "Fossil-Fueled Development (SSP5): An Energy and Resource Intensive Scenario for the 21st Century." *Global Environmental Change* 42: 297–315. https://doi.org/10.1016/j.gloenvcha.2016.05.015.

Li, S., Y. Gao, J. Zhang, et al. 2025. "Mitigating Climate Change and Ozone Pollution Will Improve Chinese Food Security." *One Earth* 8, no. 2: 101166. https://doi.org/10.1016/j.oneear.2024.12.002.

Li, X., S. Kang, J. Niu, Z. Huo, and J. Liu. 2019. "Improving the Representation of Stomatal Responses to CO_2 Within the Penman–Monteith Model to Better Estimate Evapotranspiration Responses to Climate Change." *Journal of Hydrology* 572: 692–705. https://doi.org/10.1016/j.jhydrol.2019.03.029.

Lohila, A., M. Aurela, J. Tuovinen, and T. Laurila. 2004. "Annual CO_2 Exchange of a Peat Field Growing Spring Barley or Perennial Forage Grass." *Journal of Geophysical Research: Atmospheres* 109, no. D18: 2004JD004715. https://doi.org/10.1029/2004JD004715.

Lombardozzi, D., S. Levis, G. Bonan, P. G. Hess, and J. P. Sparks. 2015. "The Influence of Chronic Ozone Exposure on Global Carbon and Water Cycles." *Journal of Climate* 28, no. 1: 292–305. https://doi.org/10.1175/JCLI-D-14-00223.1.

LRTAP Convention. 2017. "Chapter III: Mapping Critical Level for Vegetation." In *Modelling and Mapping Manual*. Federal Environmental Agency. https://icpvegetation.ceh.ac.uk.

Luo, Y., Z. Zhang, Y. Chen, Z. Li, and F. Tao. 2020. "ChinaCropPhen1km: A High-Resolution Crop Phenological Dataset for Three Staple Crops in China During 2000–2015 Based on Leaf Area Index (LAI) Products." *Earth System Science Data* 12, no. 1: 197–214. https://doi.org/10.5194/essd-12-197-2020.

Lutz, F., T. Herzfeld, J. Heinke, et al. 2019. "Simulating the Effect of Tillage Practices With the Global Ecosystem Model LPJmL (Version 5.0-Tillage)." *Geoscientific Model Development* 12, no. 6: 2419–2440. https://doi.org/10.5194/gmd-12-2419-2019.

Mao, H., E. Felker-Quinn, B. Sive, L. Zhang, Z. Ye, and H. Fang. 2024. "Examining Indicators and Methods for Quantifying Ozone Exposure to Vegetation." *Atmospheric Environment* 316: 120195. https://doi.org/10.1016/j.atmosenv.2023.120195.

Mills, G., F. Hayes, D. Simpson, et al. 2011. "Evidence of Widespread Effects of Ozone on Crops and (Semi-)natural Vegetation in Europe (1990-2006) in Relation to AOT40- and Flux-Based Risk Maps: OZONE EFFECTS ON VEGETATION IN EUROPE." *Global Change Biology* 17, no. 1: 592–613. https://doi.org/10.1111/j.1365-2486.2010.02217.x.

Mills, G., K. Sharps, D. Simpson, et al. 2018. "Ozone Pollution Will Compromise Efforts to Increase Global Wheat Production." *Global Change Biology* 24, no. 8: 3560–3574. https://doi.org/10.1111/gcb.14157.

Mintz, Y., and G. K. Walker. 1993. "Global Fields of Soil Moisture and Land Surface Evapotranspiration Derived From Observed Precipitation and Surface Air Temperature." *Journal of Applied Meteorology* 32, no.

8: 1305–1334. https://doi.org/10.1175/1520-0450(1993)032%253C1305:GFOSMA%253E2.0.CO;2.

Monfreda, C., N. Ramankutty, and J. A. Foley. 2008. "Farming the Planet: 2. Geographic Distribution of Crop Areas, Yields, Physiological Types, and Net Primary Production in the Year 2000." *Global Biogeochemical Cycles* 22, no. 1: 2007GB002947. https://doi.org/10.1029/2007GB002947.

Moureaux, C., A. Debacq, B. Bodson, B. Heinesch, and M. Aubinet. 2006. "Annual Net Ecosystem Carbon Exchange by a Sugar Beet Crop." *Agricultural and Forest Meteorology* 139, no. 1–2: 25–39. https://doi.org/10.1016/j.agrformet.2006.05.009.

O'Connor, F. 2020. *NERC UKESM1.0-LL Model Output Prepared for CMIP6 AerChemMIP* (Version 20230720) [Application/x-netcdf] Earth System Grid Federation. https://doi.org/10.22033/ESGF/CMIP6.405.

Paoletti, E., A. Alivernini, A. Anav, et al. 2019. "Toward Stomatal–Flux Based Forest Protection Against Ozone: The MOTTLES Approach." *Science of the Total Environment* 691: 516–527. https://doi.org/10.1016/j.scitotenv.2019.06.525.

Paoletti, E., and W. J. Manning. 2007. "Toward a Biologically Significant and Usable Standard for Ozone That Will Also Protect Plants." *Environmental Pollution* 150, no. 1: 85–95. https://doi.org/10.1016/j.envpol.2007.06.037.

Pastorello, G., C. Trotta, E. Canfora, et al. 2020. "The FLUXNET2015 Dataset and the ONEFlux Processing Pipeline for Eddy Covariance Data." *Scientific Data* 7, no. 1: 225. https://doi.org/10.1038/s41597-020-0534-3.

Pleijel, H., M. C. Broberg, J. Uddling, and G. Mills. 2018. "Current Surface Ozone Concentrations Significantly Decrease Wheat Growth, Yield and Quality." *Science of the Total Environment* 613: 687–692. https://doi.org/10.1016/j.scitotenv.2017.09.111.

Pleijel, H., H. Danielsson, and M. C. Broberg. 2022. "Benefits of the Phytotoxic Ozone Dose (POD) Index in Dose-Response Functions for Wheat Yield Loss." *Atmospheric Environment* 268: 118797. https://doi.org/10.1016/j.atmosenv.2021.118797.

Pleijel, H., H. Danielsson, L. Emberson, M. R. Ashmore, and G. Mills. 2007. "Ozone Risk Assessment for Agricultural Crops in Europe: Further Development of Stomatal Flux and Flux–Response Relationships for European Wheat and Potato." *Atmospheric Environment* 41, no. 14: 3022–3040. https://doi.org/10.1016/j.atmosenv.2006.12.002.

Qiao, S., S. P. Harrison, I. C. Prentice, and H. Wang. 2023. "Optimality-Based Modelling of Wheat Sowing Dates Globally." *Agricultural Systems* 206: 103608. https://doi.org/10.1016/j.agsy.2023.103608.

Ramya, A., P. Dhevagi, R. Poornima, S. Avudainayagam, M. Watanabe, and E. Agathokleous. 2023. "Effect of Ozone Stress on Crop Productivity: A Threat to Food Security." *Environmental Research* 236: 116816. https://doi.org/10.1016/j.envres.2023.116816.

Raz-Yaseef, N., D. P. Billesbach, M. L. Fischer, et al. 2015. "Vulnerability of Crops and Native Grasses to Summer Drying in the U.S. Southern Great Plains." *Agriculture, Ecosystems & Environment* 213: 209–218. https://doi.org/10.1016/j.agee.2015.07.021.

Riahi, K., D. P. Van Vuuren, E. Kriegler, et al. 2017. "The Shared Socioeconomic Pathways and Their Energy, Land Use, and Greenhouse Gas Emissions Implications: An Overview." *Global Environmental Change* 42: 153–168. https://doi.org/10.1016/j.gloenvcha.2016.05.009.

Savi, F., E. Nemitz, M. Coyle, et al. 2020. "Neural Network Analysis to Evaluate Ozone Damage to Vegetation Under Different Climatic Conditions." *Frontiers in Forests and Global Change* 3: 42. https://doi.org/10.3389/ffgc.2020.00042.

Schauberger, B., S. Rolinski, S. Schaphoff, and C. Müller. 2019. "Global Historical Soybean and Wheat Yield Loss Estimates From Ozone Pollution Considering Water and Temperature as Modifying Effects." *Agricultural and Forest Meteorology* 265: 1–15. https://doi.org/10.1016/j.agrformet.2018.11.004.

Schröder, S., M. G. Schultz, N. Selke, et al. 2021. "TOAR Data Infrastructure." FZ-Juelich B2SHARE. https://doi.org/10.34730/4D9A287DEC0B42F1AA6D244DE8F19EB3.

Sellar, A. A., C. G. Jones, J. P. Mulcahy, et al. 2019. "UKESM1: Description and Evaluation of the U.K. Earth System Model." *Journal of Advances in Modeling Earth Systems* 11, no. 12: 4513–4558. https://doi.org/10.1029/2019MS001739.

Sharps, K., F. Hayes, H. Harmens, and G. Mills. 2021. "Ozone-Induced Effects on Leaves in African Crop Species." *Environmental Pollution* 268: 115789. https://doi.org/10.1016/j.envpol.2020.115789.

Sharps, K., M. Vieno, R. Beck, F. Hayes, and H. Harmens. 2021. "Quantifying the Impact of Ozone on Crops in Sub-Saharan Africa Demonstrates Regional and Local Hotspots of Production Loss." *Environmental Science and Pollution Research* 28, no. 44: 62338–62352. https://doi.org/10.1007/s11356-021-14967-3.

Sicard, P., A. Anav, A. De Marco, and E. Paoletti. 2017. "Projected Global Ground-Level Ozone Impacts on Vegetation Under Different Emission and Climate Scenarios." *Atmospheric Chemistry and Physics* 17, no. 19: 12177–12196. https://doi.org/10.5194/acp-17-12177-2017.

Simpson, D., M. R. Ashmore, L. Emberson, and J.-P. Tuovinen. 2007. "A Comparison of Two Different Approaches for Mapping Potential Ozone Damage to Vegetation. A Model Study." *Environmental Pollution* 146, no. 3: 715–725. https://doi.org/10.1016/j.envpol.2006.04.013.

Sitch, S., P. M. Cox, W. J. Collins, and C. Huntingford. 2007. "Indirect Radiative Forcing of Climate Change Through Ozone Effects on the Land-Carbon Sink." *Nature* 448, no. 7155: 791–794. https://doi.org/10.1038/nature06059.

Stewart, J. B. 1988. "Modelling Surface Conductance of Pine Forest." *Agricultural and Forest Meteorology* 43, no. 1: 19–35. https://doi.org/10.1016/0168-1923(88)90003-2.

Tai, A. P. K., M. Sadiq, J. Y. S. Pang, D. H. Y. Yung, and Z. Feng. 2021. "Impacts of Surface Ozone Pollution on Global Crop Yields: Comparing Different Ozone Exposure Metrics and Incorporating co-Effects of CO_2." *Frontiers in Sustainable Food Systems* 5: 534616. https://doi.org/10.3389/fsufs.2021.534616.

Tang, H., J. Pang, G. Zhang, et al. 2014. "Mapping Ozone Risks for Rice in China for Years 2000 and 2020 With Flux-Based and Exposure-Based Doses." *Atmospheric Environment* 86: 74–83. https://doi.org/10.1016/j.atmosenv.2013.11.078.

Tang, Y., S. Rumbold, R. Ellis, et al. 2019. *MOHC UKESM1.0-LL Model Output Prepared for CMIP6 CMIP Historical* (Version 20230220) [Application/x-netcdf] Earth System Grid Federation. https://doi.org/10.22033/ESGF/CMIP6.6113.

Tuba, Z., K. Szente, and J. Koch. 1994. "Response of Photosynthesis, Stomatal Conductance, Water Use Efficiency and Production to Long-Term Elevated CO_2 in Winter Wheat." *Journal of Plant Physiology* 144, no. 6: 661–668. https://doi.org/10.1016/S0176-1617(11)80657-7.

Turnock, S. T., R. J. Allen, M. Andrews, et al. 2020. "Historical and Future Changes in Air Pollutants From CMIP6 Models." *Atmospheric Chemistry and Physics* 20, no. 23: 14547–14579. https://doi.org/10.5194/acp-20-14547-2020.

United Nations Department of Economic and Social Affairs, Population Division. 2022. "*World Population Prospects 2022: Summary of Results* (No. 3)." UN DESA/POP/2022/TR/NO.

Van Der, A. R. J., B. Mijling, J. Ding, et al. 2017. "Cleaning Up the Air: Effectiveness of Air Quality Policy for SO_2 and NO_x Emissions in China." *Atmospheric Chemistry and Physics* 17, no. 3: 1775–1789. https://doi.org/10.5194/acp-17-1775-2017.

Van Dingenen, R., F. J. Dentener, F. Raes, M. C. Krol, L. Emberson, and J. Cofala. 2009. "The Global Impact of Ozone on Agricultural Crop Yields Under Current and Future Air Quality Legislation." *Atmospheric*

Environment 43, no. 3: 604–618. https://doi.org/10.1016/j.atmosenv.2008.10.033.

Van Vuuren, D. P., E. Stehfest, D. E. H. J. Gernaat, et al. 2017. "Energy, Land-Use and Greenhouse Gas Emissions Trajectories Under a Green Growth Paradigm." *Global Environmental Change* 42: 237–250. https://doi.org/10.1016/j.gloenvcha.2016.05.008.

Von Bloh, W., S. Schaphoff, C. Müller, S. Rolinski, K. Waha, and S. Zaehle. 2018. "Implementing the Nitrogen Cycle Into the Dynamic Global Vegetation, Hydrology, and Crop Growth Model LPJmL (Version 5.0)." *Geoscientific Model Development* 11, no. 7: 2789–2812. https://doi.org/10.5194/gmd-11-2789-2018.

Wang, Q., M. Huang, S. Wang, et al. 2023. "Evaluation of the Impacts of Ozone on the Vegetation Productivity of Woodland and Grassland Ecosystems in China." *Ecological Modelling* 483: 110426. https://doi.org/10.1016/j.ecolmodel.2023.110426.

Wang, Y., O. Wild, K. Ashworth, et al. 2022. "Reductions in Crop Yields Across China From Elevated Ozone." *Environmental Pollution* 292: 118218. https://doi.org/10.1016/j.envpol.2021.118218.

Wesely, M. L. 1989. "Parameterization of Surface Resistances to Gaseous Dry Deposition in Regional-Scale Numerical Models." *Atmospheric Environment* 23, no. 6: 1293–1304. https://doi.org/10.1016/0004-6981(89)90153-4.

Wright, L. P., L. Zhang, I. Cheng, J. Aherne, and G. R. Wentworth. 2018. "Impacts and Effects Indicators of Atmospheric Deposition of Major Pollutants to Various Ecosystems—A Review." *Aerosol and Air Quality Research* 18, no. 8: 1953–1992. https://doi.org/10.4209/aaqr.2018.03.0107.

Yin, X., D. Rupakheti, G. Zhang, et al. 2023. "Surface Ozone Over the Tibetan Plateau Controlled by Stratospheric Intrusion." *Atmospheric Chemistry and Physics* 23, no. 17: 10137–10143. https://doi.org/10.5194/acp-23-10137-2023.

Zanis, P., D. Akritidis, S. Turnock, et al. 2022. "Climate Change Penalty and Benefit on Surface Ozone: A Global Perspective Based on CMIP6 Earth System Models." *Environmental Research Letters* 17, no. 2: 24014. https://doi.org/10.1088/1748-9326/ac4a34.

Zhang, L., J. R. Brook, and R. Vet. 2003. "A Revised Parameterization for Gaseous Dry Deposition in Air-Quality Models." *Atmospheric Chemistry and Physics* 3: 2067–2082.

Zhang, Y., M. G. Schaap, and Y. Zha. 2018. "A High-Resolution Global Map of Soil Hydraulic Properties Produced by a Hierarchical Parameterization of a Physically Based Water Retention Model." *Water Resources Research* 54, no. 12: 9774–9790. https://doi.org/10.1029/2018WR023539.

Zhou, X., X. Yue, and C. Tian. 2024. "Responses of Ecosystem Productivity to Anthropogenic Ozone and Aerosols at the 2060." *Earth's Future* 12, no. 1: e2023EF003781. https://doi.org/10.1029/2023EF003781.

Supporting Information

Additional supporting information can be found online in the Supporting Information section. **Data S1:** gcb70643-sup-0001-AppendixS1.pdf. **Data S2:** gcb70643-sup-0002-Supinfo.pdf.